Magneto-optical anisotropy study of Fe_n/Au_n superlattices

L. Uba,* S. Uba, and V. N. Antonov†
Institute of Experimental Physics, University of Bialystok, Lipowa 41, PL-15-424 Bialystok, Poland

A. N. Yaresko†
Max-Planck-Institut for the Physics of Complex Systems, D-01187 Dresden, Germany

T. Ślęzak and J. Korecki
Department of Solid State Physics, Faculty of Physics and Nuclear Techniques, University of Mining and Metallurgy, 30-059 Krakow, Poland

(Received 13 July 2000)

Extended experimental and theoretical study of the observed large magneto-optical anisotropy (MOA) is presented for a series of Fe_n/Au_n superlattices prepared by molecular beam epitaxy with $n=1,2,3$ of Fe and Au atomic planes of (001) orientation. The anisotropy of the off-diagonal component of the optical conductivity tensor with respect to the change of the magnetization direction is determined in the photon energy range 0.8–5.8 eV from the measurements of the magneto-optical polar and longitudinal saturated complex Kerr angles and the optical data measured by the spectroscopic ellipsometry. The magnitude of the observed anisotropy, decreasing with the increase of *n*, and its energy dependence are well reproduced by the band structure calculations performed within the local spin-density approximation to the density functional theory. The results of the calculations show that the microscopic origin of the large MOA is the interplay of the strong spin-orbit coupling on Au sites and the large exchange splitting on Fe sites via Au *d*-Fe *d* hybridization of the electronic states at the interfaces. The high sensitivity of the MOA to the interface structure is studied by *ab initio* modeling of the effects of substitutional disorder and the roughness at the interfaces. It is shown that a good agreement with the experiment is obtained when the interface roughness effect is taken into account. The orientation anisotropy of the *d* orbital moment is calculated from the first principles and analyzed on the basis of *d* orbital symmetry consideration. The relationship between the orbital moment anisotropy and the MOA is discussed.

I. INTRODUCTION

Many important physical properties of magnetically ordered compounds depend on the relative orientation of the magnetization and the crystallographic axes as the spin subsystem is coupled to the lattice by the spin-orbit (SO) interaction. The magnetocrystalline anisotropy (MCA), which is the energy that directs the magnetization along a certain crystallographic axis, is a ground-state property of a crystal. The magneto-optical anisotropy (MOA), defined as the dependence of the off-diagonal part of the optical conductivity tensor on the magnetization direction, arises as a result of electronic excitations and is due to the spin and orbital polarizations of initial and final states.

Although the MCA has been widely studied both experimentally[1] and theoretically[2–5] in a large number of materials, the investigations of the MOA are still restricted to a few cases only. Theoretical calculations were performed for Co, FePt, CoPt,[6] CoPd,[7] and CrO_2.[8] Experimentally, however, the orientation dependence of the magneto-optical (MO) Kerr effect was observed in only one magnetic system, hcp Co. In the equatorial Kerr effect Ganshina *et al.*,[9] and in the longitudinal Kerr effect (LKE) configuration Osgood *et al.*[10] studied the Kerr effect magnitude dependence on the orientation of the magnetization with respect to the c-axis, both lying in the basal plane of the hcp Co sample. For the polar Kerr effect (PKE) configuration with magnetization perpendicular to the sample plane, Weller *et al.*[11] observed an orientation dependence of the PKE by using two epitaxial hcp Co films with different, (0001) and $(11\bar{2}0)$, basal planes.

In the past decade, artificial multilayered structures (MLS) have attracted a lot of interest due to their unique physical properties.[1] In some cases, they exhibit simultaneously enhanced MO Kerr rotation[12] and strong interface magnetic anisotropy[13] and thus one can expect a large anisotropy of the MO response from these compounds. For several reasons it is important to investigate MLS with a small repetition period, in which individual layers consist only of few atomic layers (down to monolayers). Such systems can be easily modeled theoretically, their interfacial properties are particularly enhanced and they are precursors of artificial ordered compounds, which do not exist naturally. Especially, the low periodicity Fe/Au structures are intensively investigated experimentally[14–20] and theoretically[21–28] demonstrating unique physical properties. For the monolayer periodicity, these properties are directly connected with the formation of the $L1_0$ ordered structure, which does not exist in the Fe-Au phase diagram near equiatomic composition, but can be fabricated layer-by-layer by molecular beam epitaxy (MBE) (Refs. 15 and 18) with a high degree of perfection. The theoretical calculations[22,25] yield a strong tetragonality for the $L1_0$ Fe-Au ordered alloy, with the ratio of interlayer to intralayer lattice constant $c/a=0.90$ in the ferromagnetic state, which is in between the values expected from

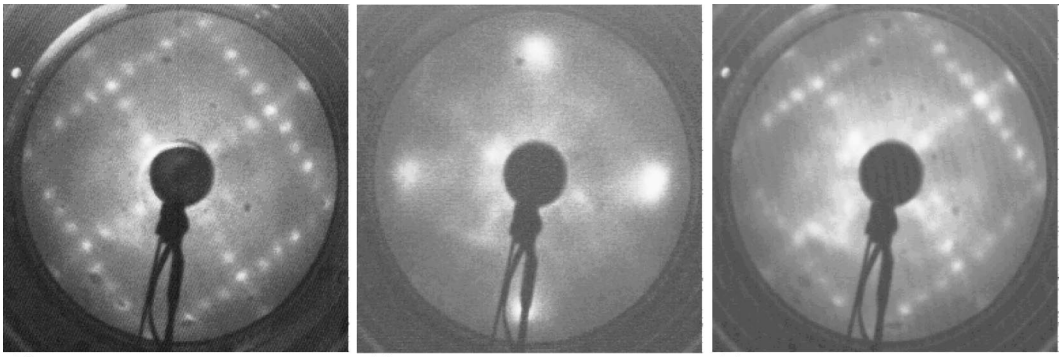

FIG. 1. LEED patterns taken during the $(Fe_2/Au_2)\times 10$ sample growth. (a) 5×1 reconstructed Au(001) buffer layer, electron energy 75 eV; (b) 1×1 pattern after completing the (Au_2/Fe_2) layers, electron energy 113 eV; (c) 5×1 reconstructed Au(001) cap layer, electron energy 75 eV.

the hard sphere model (0.86) and the experimental one (0.94).[15] Relatively low tetragonality, as observed experimentally, may result from a deviation from the layer structure, which is suggested also by the x-ray diffraction (XRD) data.[15]

Magnetic properties of the $L1_0$ ordered Fe/Au monoatomic MLS are very interesting from the application point of view, for magnetic recording. This system combines large magnetic moments and a high Curie temperature with a large uniaxial magnetic anisotropy perpendicular to Fe and Au atomic planes and specific MO Kerr spectra. The strong perpendicular anisotropy of the Fe_1/Au_1 MLS decreases rapidly for Fe_n/Au_n MLS with increasing n, so that the easy magnetization direction lies in the MLS plane already for $n=3$.[16,18] An oscillatory behavior of perpendicular anisotropy (accompanied by similar oscillations of the out-of-plane lattice spacing) is reported for n between 1 and 4, covering also nonintegers.[16,20] The MO spectra of Fe_n/Au_n MLS have been investigated experimentally and theoretically[17,20,28] in comparison with the MO spectra in ultra thin Fe layers.[29] The MLS magneto-optical spectra exhibit prominent structure in the uv spectral range, which could not be explained assuming a simple stack of thin Fe and Au layers but is related with characteristic electronic structure of the system.

The aim of this work is the detailed experimental and theoretical investigation of the orientation dependence of magneto-optical response in the Fe_n/Au_n superlattices, first observed in the Fe/Au monoatomic multilayer in Ref. 30. These structures enable us to study the specific interface effects originated from modified electronic states of the atoms at the interface by using the magneto-optical spectroscopy methods sensitive to the change of the electronic structure of the materials. The influence of the multilayer structure on the MOA is studied by the exact modeling of the effects of roughness and alloying at the interfaces. The anisotropy of the *d* orbital moment with respect to the change of the magnetization direction is calculated from the first principles and explained on the basis of *d* orbital symmetry consideration. The relationship of the orbital moment anisotropy with the MOA is discussed.

The paper is organized as follows. The detailed description of the sample preparation, experimental procedure and theoretical framework is provided in Sec. II. Experimental results and data analysis are presented in Sec. III. Section IV presents the electronic structure, the MO spectra, and the MOA of Fe_n/Au_n $(n=1,2,3)$ MLS. Finally, the results are summarized in Sec. V.

II. EXPERIMENTAL AND COMPUTATIONAL DETAILS

A. Sample preparation and experimental procedure

For the present studies, the well characterized epitaxial $(Fe_n/Au_n)\times N$ superlattices, where N is the number of repetitions and $n=1,2,3$ is the number of atomic planes, were used. The $(Fe_1/Au_1)\times 20$, $(Fe_2/Au_2)\times 10$, and $(Fe_3/Au_3)\times 7$ MLS were grown by the MBE in UHV conditions (base pressure during preparation below 5×10^{-10} mbar) on a 30 nm (001)Au buffer layer (preceded by a 4 nm Fe(001) seed layer), deposited on a MgO(001) cleaved substrates in a multistage process.[31] The whole structure was finally covered by a 5 nm Au cap-layer. The Fe and Au monolayers were deposited alternately at 340 K at the rate of about 0.2 nm/min, as controlled by a quartz microbalance with an accuracy of $\pm 5\%$. The sample growth was monitored *in situ* by low energy electron diffraction (LEED), which has documented epitaxial growth with the (001) orientation across the whole sample, as it is exemplified in Fig. 1 for the $(Fe_2/Au_2)\times 10$ MLS. The (5×1) reconstruction of the Au(001) buffer layer surfaces [Fig. 1(a)] is lifted upon the deposition of about 0.5 monolayer (ML) of Fe and a (1×1) LEED pattern with relatively broad spots is observed after completion of the Fe sublayers [Fig. 1(b)]. The (5×1) reconstruction restores for each Au sublayers already within 1 ML of Au and it is seen also for the Au caplayers [Fig. 1(c)] proving a perfect epitaxy, comparable with that of the buffer layer. Thus, very uniform growth conditions are preserved for subsequent layers, resulting in a high epitaxial quality of the superlattices. For the growth mode and the resulting structure of the Fe/Au MLS an important role plays the Au self-surfactant effect, which was observed when single Fe films were grown on the reconstructed (001)Au surface.[31,32] During the Fe growth, the Au surface segregation occurs by an atomic place exchange that leads to the formation of one Au monolayer on top of the growing Fe film. This process, particularly important for the growth of the Fe_1/Au_1 monoatomic superlattices, is responsible for a deviation from a perfect layer structure as it was observed by Takanashi

et al.[15] by XRD measurements. Local structural and electronic properties of the Fe/Au MLS used for the present studies could be characterized precisely by the conversion electron Mössbauer spectroscopy (CEMS), because our samples were made of the isotopically pure ^{57}Fe. The CEMS analysis[18] clearly reveals that the $L1_0$ phase, characterized by the tetragonal distortion that is reflected in a large contribution of the quadrupole interaction to the hyperfine pattern, is present in the $(Fe_1/Au_1)\times 20$ MLS. However, the amount of the $L1_0$ phase is only $\sim$30% of that expected for the perfect layer growth. The vertical mass transport accompanying the MLS growth leads to Fe aggregation, so that the resulting structure may be regarded as a mixture of a monolayer and double-layer (and to a less extent also trilayer) MLS. Nevertheless, it is enough to induce a strong perpendicular anisotropy, which forces the magnetization to the normal direction. The $L1_0$ phase disappears abruptly when the MLS modulation period is increased. For the $(Fe_2/Au_2)\times 10$ MLS, only traces of the component attributed to the tetragonally distorted phase can be found in the CEMS spectrum. The CEMS spectrum for the $(Fe_3/Au_3)\times 7$ sample resembles the one measured for a single Fe trilayer film sandwiched between Au.[18]

In the present work magneto-optical polar Kerr rotation (θ^{PK}) and ellipticity (η^{PK}), and longitudinal Kerr rotation (θ^{LK}) and ellipticity (η^{LK}) spectra were measured at room temperature with a high sensitivity reaching the 10^{-5}–10^{-4} deg range, for the photon energy from 0.8 to 5.8 eV in an improved experimental setup as compared to that described in Ref. 33. The spectroscopic measurements in both polar and longitudinal magnetization configurations were based on a polarization modulation technique with the use of a photoelastic modulator (PEM CaF_2). The angle of incidence of the light beam on the sample mounted inside closed core electromagnets was set at 2 and 75 deg in the polar and longitudinal geometry, respectively. After reflection from the sample the light beam passed through an analyzer with its transmission axis set at 0 or 90 deg to the plane of incidence for *p* and *s* polarization, respectively. In the energy range 0.8–1.5 eV a low-noise sensitive InGaAs photodiode, and in the range of 1.5–5.8 eV, VIS- and UV- sensitive photomultipliers were used for the detection of light intensity. The magnetic field available was 16 kOe in the longitudinal geometry and 18 kOe in the polar geometry and was enough to saturate the samples in both configurations, as it was derived from the measured magneto-optical hysteresis loops at fixed wavelengths. The optical properties—refractive index *n* and extinction coefficient *k*—were measured directly by spectroscopic ellipsometry with the use of a rotating analyzer method in the energy range 0.8–5.8 eV.

B. Computational details

Phenomenologically, magneto-optical effects at optical frequencies are treated by means of a dielectric tensor. For the polar Kerr magnetization geometry and a crystal of tetragonal symmetry, where both the fourfold axis and the magnetization direction are perpendicular to the sample surface and the *z*-axis is chosen to be parallel to them, the dielectric tensor is composed of the diagonal ε_{xx} and ε_{zz}, and the off-diagonal ε_{xy} component in the form

$$\boldsymbol{\varepsilon}=\begin{pmatrix} \varepsilon_{xx} & \varepsilon_{xy} & 0 \\ -\varepsilon_{xy} & \varepsilon_{xx} & 0 \\ 0 & 0 & \varepsilon_{zz} \end{pmatrix}. \tag{1}$$

At normal light incidence the relation between the polar complex Kerr angle and the dielectric tensor components is given by[34]

$$\theta^{PK}+i\,\eta^{PK}=\frac{-\varepsilon_{xy}}{(\varepsilon_{xx}-1)\sqrt{\varepsilon_{xx}}}, \tag{2}$$

where θ^{PK} and η^{PK} are the polar Kerr rotation and the ellipticity, respectively.

Here and henceforth, the following definitions have been adopted. We choose the time dependence of the electric field as $e^{-i\omega t}$. Hence, all the complex quantities are expressed by their real and imaginary parts as follows: $\varepsilon_{\alpha\beta}=\varepsilon^{(1)}_{\alpha\beta}+i\varepsilon^{(2)}_{\alpha\beta}$, where $\alpha,\beta\equiv x,y,z$, $\varepsilon_{xx}=(n+ik)^2$, and *n* and *k* are refractive index and extinction coefficient, respectively. The optical conductivity tensor $\sigma_{\alpha\beta}=\sigma^{(1)}_{\alpha\beta}+i\sigma^{(2)}_{\alpha\beta}$ is related to the dielectric tensor $\varepsilon_{\alpha\beta}$ through the equation

$$\varepsilon_{\alpha\beta}(\omega)=\delta_{\alpha\beta}+\frac{4\pi i}{\omega}\sigma_{\alpha\beta}(\omega). \tag{3}$$

For the longitudinal Kerr magnetization geometry, where the magnetization lies in the sample plane and the *y*-axis is chosen to be parallel to both the direction of the magnetization and the plane of incidence, the dielectric tensor takes the form

$$\boldsymbol{\varepsilon}=\begin{pmatrix} \varepsilon_{xx} & 0 & -\varepsilon_{xz} \\ 0 & \varepsilon_{xx} & 0 \\ \varepsilon_{xz} & 0 & \varepsilon_{zz} \end{pmatrix}. \tag{4}$$

The formula for the longitudinal complex Kerr angle as it has been derived from general formulas for the Kerr effect with arbitrary dielectric tensor[35] is given by

$$\theta^{LK}_{s,p}+i\,\eta^{LK}_{s,p}=-\frac{2\varepsilon_{xz}\sin\varphi\cos\varphi\sqrt{\varepsilon_{xx}}}{D}, \tag{5}$$

with

$$\begin{aligned} D=&\left(\sqrt{\varepsilon_{xx}(\varepsilon_{zz}-\sin^2\varphi)}+\sqrt{\varepsilon_{zz}(\varepsilon_{xx}-\sin^2\varphi)}\right)\\ &\times\left(\sqrt{\varepsilon_{xx}-\sin^2\varphi}\pm\cos\varphi\right)\\ &\times\left(\sqrt{\varepsilon_{xx}\varepsilon_{zz}}\cos\varphi\mp\sqrt{\varepsilon_{zz}-\sin^2\varphi}\right), \end{aligned}$$

where φ is the angle of light incidence, and the upper and lower signs correspond to the *p* and *s* light polarization, parallel and perpendicular to the plane of incidence, respectively.

In the case when the assumption $\varepsilon_{zz}\approx\varepsilon_{xx}$ is justified the formula (5) simplifies to[36]

$$\theta^{LK}_{s,p}+i\,\eta^{LK}_{s,p}=-\frac{\varepsilon_{xz}\sin\varphi\left(\sqrt{\varepsilon_{xx}-\sin^2\varphi}\pm\sin\varphi\tan\varphi\right)}{(\varepsilon_{xx}-1)(\varepsilon_{xx}-\tan^2\varphi)\sqrt{\varepsilon_{xx}-\sin^2\varphi}}. \tag{6}$$

Using straightforward symmetry considerations it can be shown that all MO phenomena are caused by the symmetry reduction, in comparison to the paramagnetic state, caused by magnetic ordering.[37] Concerning optical properties this symmetry reduction only has consequences when SO coupling is considered in addition. To calculate MO properties one therefore has to account for magnetism and SO coupling at the same time when dealing with the electronic structure of the material considered. Performing corresponding band structure calculations, it is normally sufficient to treat SO coupling in a perturbative way. A more rigorous scheme, however, is obtained by starting from the Dirac equation set up in the framework of relativistic spin density functional theory:[38]

$$[c\boldsymbol{\alpha}\cdot\mathbf{p}+\boldsymbol{\beta}mc^2+\boldsymbol{I}V+V_{sp}\boldsymbol{\beta}\boldsymbol{\sigma}_z]\psi_{n\mathbf{k}}=\epsilon_{n\mathbf{k}}\psi_{n\mathbf{k}} \tag{7}$$

with $V_{sp}(\mathbf{r})$ being the spin-polarized part of the exchange-correlation potential corresponding to the z quantization axis. All other parts of the potential are contained in $V(\mathbf{r})$. The 4×4 matrices $\boldsymbol{\alpha}$, $\boldsymbol{\beta}$, and $\boldsymbol{I}$ are defined by

$$\boldsymbol{\alpha}=\begin{pmatrix}0 & \boldsymbol{\sigma}\\ \boldsymbol{\sigma} & 0\end{pmatrix},\quad \boldsymbol{\beta}=\begin{pmatrix}\mathbf{1} & 0\\ 0 & -\mathbf{1}\end{pmatrix},\quad \boldsymbol{I}=\begin{pmatrix}\mathbf{1} & 0\\ 0 & \mathbf{1}\end{pmatrix}, \tag{8}$$

where $\boldsymbol{\sigma}$ are the standard Pauli matrices, and $\mathbf{1}$ is the 2×2 unit matrix.

There are quite a few band structure methods available now that are based on the above Dirac equation.[44] In one of the schemes the basis functions are derived from the proper solution of the Dirac equation for the spin dependent single-site potentials.[39,40] In another one, the basis functions are obtained initially by solving the Dirac equation without the spin-dependent term[41,42] and then this term is accounted for in the variational step.[43,39] In spite of this approximation, the latter scheme gives the results in a close agreement with the former,[44] while being simpler to implement. We should also mention the widely used technique in which the SO coupling is added variationally[41] after the scalar relativistic magnetic Hamiltonian has been constructed. In this case, the Pauli equation with the SO coupling is solved instead of the Dirac equation. We should emphasize that all three techniques yield similar results.

The optical conductivity tensor or equivalently, the dielectric tensor is the basic spectral quantity needed for the evaluation of the Kerr effect.[45] The optical conductivity can be computed from the energy band-structure by means of the Kubo-Greenwood linear-response expression:[46,47]

$$\sigma_{\alpha\beta}(\omega)=\frac{-ie^2}{m^2\hbar V_{uc}}\times\sum_{\mathbf{k}}\sum_{nn'}\frac{f(\epsilon_{n\mathbf{k}})-f(\epsilon_{n'\mathbf{k}})}{\omega_{nn'}(\mathbf{k})}\frac{\Pi^{\alpha}_{n'n}(\mathbf{k})\Pi^{\beta}_{nn'}(\mathbf{k})}{\omega-\omega_{nn'}(\mathbf{k})+i\gamma}, \tag{9}$$

where $f(\epsilon_{n\mathbf{k}})$ is the Fermi function, $\hbar\omega_{nn'}(\mathbf{k})\equiv\epsilon_{n\mathbf{k}}-\epsilon_{n'\mathbf{k}}$ is the energy difference of the Kohn-Sham energies $\epsilon_{n\mathbf{k}}$, and γ is the lifetime parameter, which is included to describe the finite lifetime of excited Bloch electron states. The $\Pi^{\alpha}_{nn'}$ are the dipole optical transition matrix elements, which in a fully relativistic description are given by[48]

$$\boldsymbol{\Pi}_{nn'}(\mathbf{k})=m\langle\psi_{n\mathbf{k}}|c\boldsymbol{\alpha}|\psi_{n'\mathbf{k}}\rangle \tag{10}$$

with $\psi_{n\mathbf{k}}$ being the four-component Bloch electron wave functions.

Equation (9) for the conductivity contains a double sum over all energy bands, which naturally separates in the so-called interband contribution, i.e., $n\neq n'$, and the intraband contribution, $n=n'$. The intraband contribution to the diagonal components of $\boldsymbol{\sigma}$ may be rewritten for zero temperature as

$$\sigma_{\alpha\alpha}(\omega)\equiv\frac{(\omega_{p,\alpha})^2}{4\pi}\frac{i}{\omega+i\gamma_D}, \tag{11}$$

where $\omega_{p,\alpha}$ are the components of the plasma frequency, which are given by

$$(\omega_{p,\alpha})^2\equiv\frac{4\pi e^2}{m^2V_{uc}}\sum_{n\mathbf{k}}\delta(\epsilon_{n\mathbf{k}}-E_F)|\Pi^{\alpha}_{nn}|^2, \tag{12}$$

E_F is the Fermi energy, and $\gamma_D=1/\tau_D$ where τ_D is the phenomenological Drude electron relaxation time. The intraband relaxation time parameter γ_D may be different from the interband relaxation time parameter γ. The latter can be frequency dependent,[49] and, because excited states always have a finite lifetime, will be nonzero, whereas γ_D will approach zero for very pure materials. For the interband relaxation parameter we shall use, unless stated otherwise, $\gamma=1$ eV. This value has been found to be on average a good estimate of this phenomenological parameter. The contribution of intraband transitions to the off-diagonal conductivity is usually not considered. Also, we did not study the influence of local field effects on the MO properties. We mention, lastly, that the Kramers-Kronig transformation was used to calculate the dispersive parts of the optical conductivity from the absorptive parts.

In our band structure calculations we consider Fe_1/Au_1 MLS system with one by one stacking of (001) planes whose structure can be regarded as $L1_0$ type [Fig. 2(a)]. The lattice parameters used were chosen as follows. The in-plane atomic spacing was taken as an average between Au and Fe bulk values ($a=4.066$ Å). The out-of-plane lattice spacing for the Fe_1/Au_1 MLS was taken from the recent work of Sato *et al.*[20] as 1.915 Å which is a slightly lower value as compared to the previously published one[15,16] and used in our previous calculation.[30] The structures Fe_2/Au_2 and Fe_3/Au_3 are presented in Figs. 2(b) and 2(c). There is no experimental knowledge about the three interlayer spacings, Au-Au, Au-Fe, and Fe-Fe, in these structures. The Au-Au spacing was taken the same as in fcc Au, 2.04 Å. For the Au-Fe spacing, value of 1.74 Å can be derived from the rigid sphere model as a mean between the fcc Au (2.04 Å) and bcc Fe (1.43 Å) bulk values. Similar values for the Au-Fe interlayer spacings we have obtained by total energy minimization using the LMTO *ab initio* calculations. Using the experimentally determined superlattices periods in Fe_2/Au_2 and Fe_3/Au_3 MLS structures published in Ref. 20 as constrains, the one-parameter minimization was performed. As a result, the values of 1.76 Å and 1.74 Å for Au-Fe, and corresponding val-

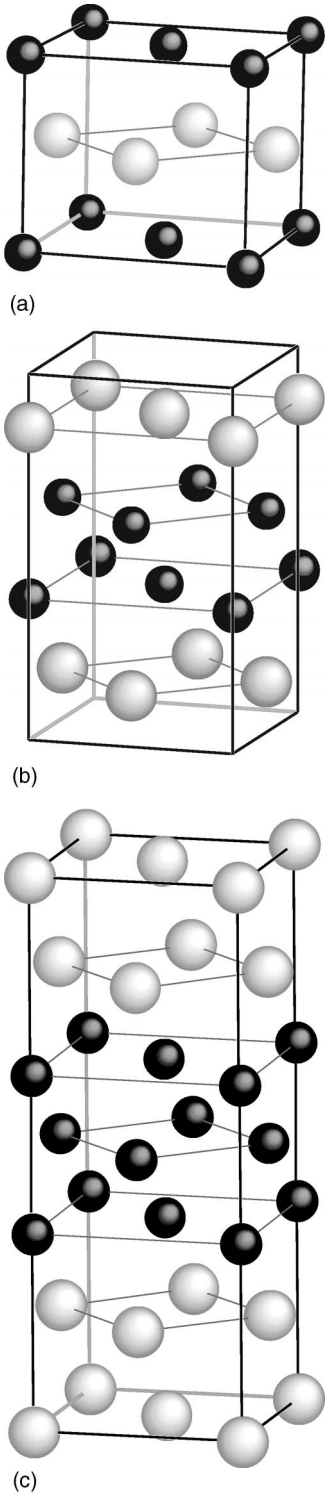

FIG. 2. The unit cells used for Fe_1/Au_1 ($L1_0$) (a), Fe_2/Au_2 (b), and Fe_3/Au_3 MLS (c). Black spheres are Fe atoms and shadowed ones are Au atoms.

ues of 1.69 and 1.58 Å for Fe-Fe interlayer spacing in the Fe_2/Au_2 and Fe_3/Au_3 MLS, respectively, were obtained.

The details of the computational method are described in our previous paper[33] and here we only mention several aspects. The electronic structure of the compounds was calculated self-consistently on the basis of the local spin density approximation[50] to the density functional theory using the fully relativistic spin-polarized LMTO method[41–43] in the

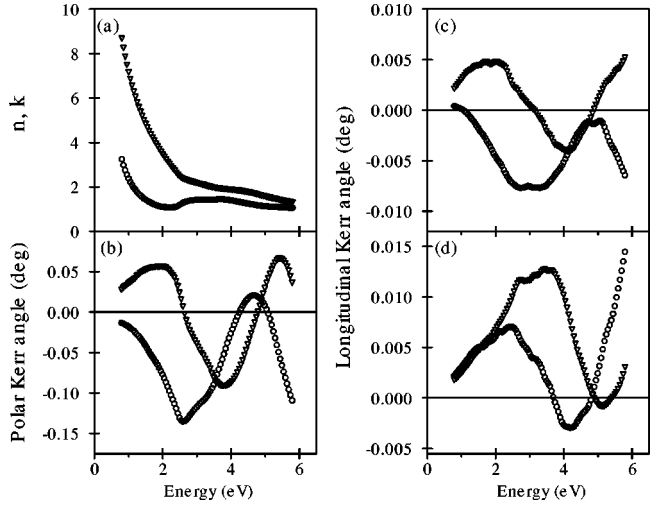

FIG. 3. Experimental results for Fe_1/Au_1 MLS: refractive index and extinction coefficient (a), polar Kerr rotation and ellipticity (b), longitudinal Kerr rotation and ellipticity for *s* (c) and *p* (d) light polarizations. In the panels, refractive index and rotation are depicted as circles, and extinction coefficient and ellipticity as triangles.

atomic-sphere approximation, including the combined correction (ASA+CC).[41,51] Core-charge densities were recalculated at every iteration of the self-consistency loop. The spin polarization was included in the variational step.[39] The combined correction terms were also taken into account in the optical matrix element calculations.[48] The basis consisted of *s*, *p*, *d*, and *f* LMTO's for both Fe and Au was used. The **k**-space integrations were performed with the improved tetrahedron method[52] and charge self-consistency was achieved with 2176, 1155, and 702 irreducible **k**-points for Fe_1/Au_1, Fe_2/Au_2, and Fe_3/Au_3 MLS, respectively.

III. EXPERIMENTAL RESULTS AND DATA ANALYSIS

Most MO studies of the MLS employ polar magnetization geometry, PKE, and normal light incidence. The PKE configurations alone cannot be used, however, to study the MO orientation effects in a very rich family of magnetic layered structures. The reason is that the main structural anisotropy axis is the axis perpendicular to the film surface and no other basal planes exist. The only possibility is to use the polar and longitudinal (or equatorial) Kerr effect geometries simultaneously. This approach is more complicated as additional data on the optical constants are required to extract the basic quantities—optical conductivity tensor components—underlying the MO spectra.

In Fig. 3 the complete set of experimentally obtained ellipsometric and magneto-optical spectra in both the polar and longitudinal magnetization geometry for the Au(5 nm)/$(Fe_1/Au_1)\times 20$/Au(30 nm)/Fe(4 nm)/MgO(001) sample is presented. As it is seen in Fig. 3(a), the spectral dependence of the effective refractive index *n* and the extinction coefficient *k* of the sample exhibits overall shape close to that of Au metal with the well known feature at the photon energy of 2.5 eV, where there is the superposition of the Drude-like intraband transitions and the interband transition edge. Such dependence can easily be understood by taking into account

that the predominant parts of the sample are the Au overlayer and underlayer. The effective magneto-optical PKE rotation θ^{PK} and ellipticity η^{PK} spectra of the sample are shown in Fig. 3(b). The essential points of the experimental θ^{PK} spectrum are the prominent negative peak centered at around 2.5 eV (i.e., in the Au plasma edge spectral region), and a hump clearly visible near 3.2 eV. The θ^{PK} changes a sign above 4 eV and a positive peak at 4.7 eV is formed. The θ^{PK} enhancement at the plasma edge of Au (around 2.5 eV) is well explained by the classical optic multilayer model, and is not related to the modification of the electronic structure of the intrinsic magnetic Fe_1/Au_1 multilayer. The corresponding η^{PK} spectrum changes the sign at the energy of the plasma edge of Au and in the uv spectral region exhibits two peak structure with a negative peak at 3.8 eV and a positive one at 5.5 eV. The PKE spectra measured in the Fe_2/Au_2 and Fe_3/Au_3 superlattices (not shown) exhibit similar behavior like Fe_1/Au_1 one, with the peaks structure in the uv spectral range shifted to higher energy. The main features and trends in PKE spectra of Fe_n/Au_n superlattices modulated by integer atomic layers of the Fe and Au are in agreement with those reported in Refs. 17 and 20. Similar characteristic structure in the PKE spectra in the uv spectral range (more distinct than in the multilayers) was observed in ultrathin Fe layers sandwiched by Au layers and assigned to optical transitions involving quantum-well states.[29,53]

The corresponding complex LKE spectra measured in the longitudinal Kerr magnetization geometry at the angle of light incidence 75 deg are shown in Fig. 3(c) and Fig. 3(d) for *s* and *p* light polarizations, respectively. The measured θ^{LK} and η^{LK} appear one order in magnitude smaller than for the PKE. In the LKE spectra, the plasma edge of Au overlayer and underlayer of the sample manifests itself as a peak or shoulder near 2.6 eV. As it is seen in Fig. 3(c) and 3(d), in the spectral region above 2.5 eV the θ^{LK} spectra are dominated by the peak at 3.2 and minimum around 5.0 eV for *s* and the peak at 4.1 eV for *p* polarization, respectively. The corresponding η^{LK} spectra features are the peak centered at 4.1 for *s* and the peaks at 3.4 and 5.1 eV for *p* polarization, respectively. The LKE spectra are consistent for the *s* and *p* light polarizations and the optical functions *n* and *k* determined from the LKE data alone agree well with those measured directly by the elipsometric method. It should be pointed out that one can not expect direct correspondence between the spectra shape and energy peaks position measured in polar and longitudinal geometry because the LKE spectra are strongly dependent on the angle of light incidence (particularly for *p* polarization, when the angle of incidence approaches its principal value, equal to about 75 deg for the structures studied). Therefore, the direct comparison of the PKE and LKE spectra is not adequate and appropriate treatment should be done by evaluation of the optical conductivity tensor components from the measured spectra. It is well known that the absorptive part of the tensor only, but not the Kerr rotation itself, is directly connected with the optical transitions between electronic states, their strengths and energy positions. Therefore, in the following, we will consider the energy dependence of the conductivity tensor components underlying the MO effects for the superlattices studied.

The effective optical conductivity tensor components, diagonal σ_{xx}^{eff} and off-diagonal $\omega\sigma_{xy}^{eff}$, $\omega\sigma_{xz}^{eff}$ were determined

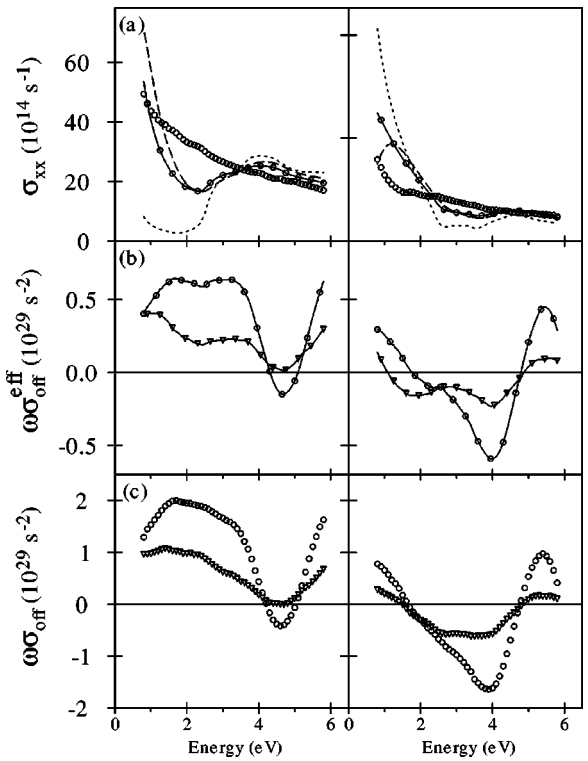

FIG. 4. Experimental absorptive (left panels) and dispersive (right panels) parts of the optical conductivity for the Fe_1/Au_1 sample. In the panels (a) the effective diagonal tensor components of the whole sample (solid lines with circles), the buffer sample (dashed lines), thick Au film (dotted lines), and the extracted (see text) component of the intrinsic Fe_1/Au_1 structure (circles) are shown. In the panels (b) the off-diagonal effective tensor components derived from the polar (solid lines with circles) and longitudinal (solid lines with triangles) Kerr effect are shown. In the panels (c) there are the extracted off-diagonal tensor components of the intrinsic magnetic Fe_1/Au_1 structure derived from PKE (circles) and LKE (triangles).

with the use of Eq. (3) from the measured optical and MO spectra according to the Eq. (2) for the PKE and Eq. (6) for the LKE. The Fe_n/Au_n superlattices studied are two-dimensional structures and can exhibit optical anisotropy (i.e., the σ_{xx} and σ_{zz} tensor components can differ). Consequently, Eq. (5) for an optically anisotropic medium should be used instead of Eq. (6) to determine the off-diagonal tensor component. Unfortunately, in the case of thin *metallic* films or MLS direct ellipsometric measurements allow to determine the σ_{xx}^{eff} tensor component only. As it will be shown in the next section, the errors caused by using Eq. (6) for an optically isotropic medium to extract σ_{xz}^{eff} from LKE data are of little importance for the Fe_n/Au_n MLS.

The results for effective complex σ_{xx}^{eff}, $\omega\sigma_{xy}^{eff}$, and $\omega\sigma_{xz}^{eff}$ optical conductivity spectra of the Au(5 nm)/$(Fe_1/Au_1)\times 20$/Au(30 nm)/Fe(4 nm)/MgO(001) sample are presented in Fig. 4(a) and 4(b), respectively. In Fig. 4(a), the σ_{xx} spectra of 100 nm thick fcc Au film deposited on GaAs(001) as well as the buffer sample Au(30 nm)/Fe(4 nm)/MgO(001) used as the substrate to grow the Fe_n/Au_n superlattices are also included. As can be seen from Fig. 4(a) there is significant difference between the effective σ_{xx}^{eff} spectra for the whole structure and the buffer sample as com-

pared to that of the Au film in the spectral range below 2.5 eV. The rapid changes of the optical constants at the energy 2.5 eV caused by onset of Au interband transitions are clearly visible for all the samples. The characteristic features of the absorptive part of the $\omega\sigma_{xy}^{eff}$ spectrum [Fig. 4(b), solid lines with circles] of the whole structure are two broad peaks of comparable amplitude centered at around 1.6 and 3.3 eV and a negative minimum at 4.7 eV. The dispersive part of the $\omega\sigma_{xy}^{eff}$ is dominated by a negative peak at 3.9 eV and a positive one at 5.3 eV. The complex $\omega\sigma_{xz}^{eff}(\omega)$ functions [Fig. 4(b), solid lines with triangles] evaluated independently from the LKE data measured for *s* and *p* light polarization are the same. As compared to the energy dependence of $\omega\sigma_{xy}^{eff}(\omega)$, significant differences between the spectra shape and magnitude are clearly visible. The ir peak position in the absorptive part of $\omega\sigma_{xz}^{eff}$ shifts to lower energy and the spectrum amplitude is much smaller.

The conductivity tensor components spectra discussed above represent the effective tensor components of the whole complex sample composed of the specific magnetic Fe_n/Au_n structure and the Au cap layer and underlayer film. To compare the theoretical *ab initio* calculations with the experiment and to discuss the origin of the magneto-optical and MOA effects of the magnetic superlattices, the tensor components for the intrinsic magnetic Fe_n/Au_n structure alone should be extracted from the experimental data. For this aim, we adopted the phenomenological matrix formalism based on the Maxwell theory providing computer modeling of the MO response for a given structure (known as multireflection calculation).[54] The procedure assumes that the dielectric tensors of the constituent layers of the structure and their thicknesses are known. In our calculation, the thicknesses of the constituent layers determined from the technological data were used. To avoid possible uncertainties and obtaining the best precise results, the optical and magneto-optical response of the buffer underlying the Fe_n/Au_n structure, composed of the Au(30 nm)/Fe(4 nm)/MgO(001), was directly measured with the use of the control sample and further used in the multireflection calculations. Finally, we consider a two-layer system composed of the nonmagnetic Au cover layer and the magnetic $(Fe_n/Au_n)\times N$ superlattice on the Au(30 nm)/Fe(4 nm)/MgO(100) buffer substrate. In the procedure, the contribution of a single layer of given thickness is determined through its characteristic matrix, composed of the medium boundary and the medium propagation matrices.[54] The overall structure of the film is treated as a single layer with the parameters expressed in terms of those of individual sublayers.

The unknown tensor components of the intrinsic $(Fe_1/Au_1)\times N$ MLS structure were extracted by solving numerically multireflection equations. The results for the Fe_1/Au_1 structure are shown in Fig. 4(a) for σ_{xx} (circles) and in Fig. 4(c) for $\omega\sigma_{xy}$ (circles) and $\omega\sigma_{xz}$ (triangles). The spectra represent the results after eliminating the MO contribution from the complex underlayer and Au overlayer. In the following discussion, the off-diagonal component $\omega\sigma_{xy}$ for the magnetization **M** parallel to the (001) direction will be denoted as $\omega\sigma_{\rm off}^{\parallel}$, whereas for the $\omega\sigma_{xz}$ with the magnetization **M** perpendicular to the (001) direction we will use the notation $\omega\sigma_{\rm off}^{\perp}$. As compared to the effective tensor components, the feature related to the plasma edge of Au at 2.5 eV disappears for $\omega\sigma_{\rm off}^{\parallel}$ and $\omega\sigma_{\rm off}^{\perp}$ spectra. The overall structure of the extracted off-diagonal tensor components of the magnetic superlattice alone is similar to that of the effective ones and the most significant changes in the spectra appear in the ir spectral range. The most important conclusion is that both the effective and the extracted off-diagonal tensor components of the magnetic superlattice exhibit large orientational anisotropy with respect to the magnetization direction.

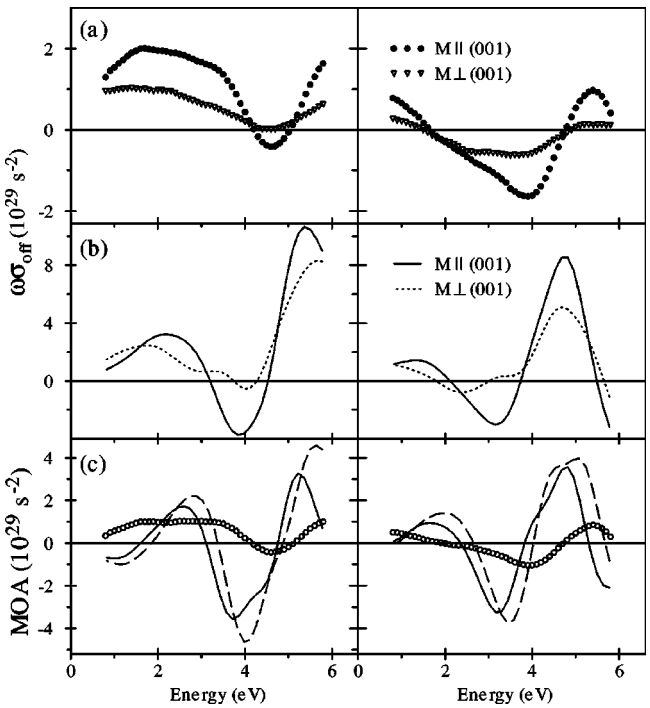

FIG. 5. Absorptive (left panels) and dispersive (right panels) parts of the off-diagonal conductivity tensor of Fe_1/Au_1 MLS; (a) experimental results, (b) LSDA calculated spectra for Fe_1/Au_1 MLS, (c) the MO anisotropy spectra (symbols represent experimental data, solid lines LSDA, and dashed lines LDA+U theory).

IV. MAGNETO-OPTICAL ANISOTROPY IN Fe_n/Au_n SUPERLATTICES

A. Comparison of the experimental and theoretical spectra in Fe_n/Au_n MLS

For the quantitative analysis of the magneto-optical anisotropy it is convenient to present the anisotropy as the difference between the off-diagonal conductivity tensor components $\omega\sigma_{\rm off}^{\parallel}-\omega\sigma_{\rm off}^{\perp}$, where the factor ω provides the compatibility with the $\omega\sigma$ spectra themselves. In Fig. 5 the $\omega\sigma_{\rm off}^{\parallel}$ and $\omega\sigma_{\rm off}^{\perp}$ spectra of the MLS of nominal Fe_1/Au_1 structure, extracted from the experimental PKE and LKE data as described in the previous section, and the MOA are compared to the corresponding spectra calculated for the ideal Fe_1/Au_1 $L1_0$ structure.

Overall, both the spectral shape and the magnitude of the experimental optical conductivity spectra are qualitatively reproduced by the LSDA calculations. However, the position of the calculated prominent peaks in absorptive part of $\omega\sigma_{\rm off}^{\parallel}$ at 3.8 eV and 5.2 eV is shifted towards smaller energies as compared to the experiment. Also, the theoretical calcula-

tions predict larger MOA in comparison with the experimental one in the nominal Fe_1/Au_1 structure. One of the possible reasons is that due to the non-exact treatment of the electron exchange and correlations the LSDA underestimates the binding energy of *d* states and the threshold of interband transitions in noble metals compared to photoemission and optical measurements.[55,56]

It seems quite likely that the use of a more appropriate approximation for the self-energy can give rise to a shift of the quasiparticle energy bands originated from Au $5d$ states and, as a result, to a better agreement between the theory and the experiment. In the present work the LDA+U method[57] has been adopted as a step beyond the LSDA in the treatment of the electronic correlations. As it was discussed in Refs. 58 and 59, the LDA+U method can be considered as a rough approximation to both the self-interaction correction and to the self-energy of a system with strongly interacting electrons. Moreover, it has been found that the application of the LDA+U method to pure noble metals allows to improve the calculated energy position of the threshold of the interband optical transitions and provides a better approach in description of their MO spectra.[60] In the present case of the Fe_1/Au_1 MLS $U_{eff}=2.5$ eV was applied to Au $5d$ states. This value of U_{eff}, considered as a parameter of the model, was found to give the best agreement between the calculated and experimental optical conductivity for fcc Au. The use of the LDA+U approximation for Fe_1/Au_1 MLS does improve slightly the calculated energy position of the peaks of the off-diagonal optical conductivity for both orientations of the magnetization (not shown), there is no improvement, however, in the shape of the spectra. Comparing the MOA calculated within LSDA and LDA+U methods [see Fig. 5(c)] to the experimental spectrum one can conclude that the LDA+U approximation does not improve the description of the MOA in the nominal Fe_1/Au_1 structure.

Another and maybe even more important source of the discrepancies is that the studied sample is not an ideal monoatomic Fe_1/Au_1 MLS of $L1_0$ structure but rather a mixture of mono- and double-layer structures. Having this in mind we modeled the effective optical conductivity of the structure by a weighted average of the conductivities calculated for the Fe_1/Au_1 and Fe_2/Au_2 MLS: $\omega\sigma_{\rm off}=x\cdot\omega\sigma_{\rm off}^{1/1}+(1-x)\cdot\omega\sigma_{\rm off}^{2/2}$. The best agreement between the theory and the experiment, both in the MOA [Fig. 6(a)] and the shape of the off-diagonal optical conductivity (not shown) was achieved with $x=0.3$. This value agrees well with the results of the CEMS analysis.[18]

In a more advanced approach, we studied the interface roughness by calculating the MO properties of the mixture of mono- and double layers, distributed over the whole structure. We modeled the composed Fe/Au structure using a large supercell containing the side-by-side placed Fe_1/Au_1 and Fe_2/Au_2 component structures spread over 3 and 7 lattice constants (see Fig. 7). This ratio of the areas was chosen in a correspondence to the simple procedure described above, in which the resulting spectra were expressed as the sum of individual Fe_1/Au_1 and Fe_2/Au_2 contributions. The results of the *ab initio* calculations for the composed structure are shown in Fig. 6(a), from which an even better overall agreement between the theory and experiment both in the shape and the amplitude of the MOA spectra is observed. As

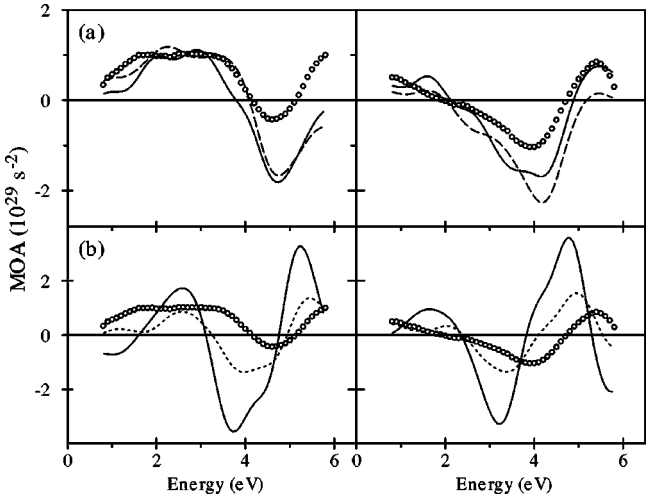

FIG. 6. Absorptive (left panels) and dispersive (right panels) part of the MOA measured for the Fe_1/Au_1 MLS (circles) compared with LSDA calculated spectra; (a) MOA modeled with effective optical conductivity: $\omega\sigma_{\rm off}=x\cdot\omega\sigma_{\rm off}^{1/1}+(1-x)\cdot\omega\sigma_{\rm off}^{2/2}$ for $x=0.3$ (solid lines) and calculated for supercell containing 1/1 and 2/2 substructures (see Fig. 7) (dashed lines); (b) MOA calculated for perfect Fe_1/Au_1 structure (solid lines) and for the structure with the substitutional disorder (see Fig. 8) (dotted lines).

the opposite case to the structure composed of well-defined mono- and double-layers, we performed a series of modeling in which we examined the effect of substitutional disorder on the MO spectra and MOA. Although the solubility of Au in bulk bcc Fe at the temperature up to 400 K is negligible,[61] enhanced solubility of Au within the Fe layer up to 3% was observed for 70 Å thick Fe film on Au(001).[62] Even up to one order greater substitutional disorder was reported for the Fe/Au (001) structures in the monolayer regime by Blum *et al.*[32] The incorporation of Au atoms in the Fe layers can be considered as an explanation (as discussed in Ref. 32) for larger Fe-Au interlayer spacing observed experimentally in Fe_1/Au_1 structure, as compared to the spacings derived under assumption of rigid atomic spheres of bulk Fe and Au metals. The effect will lead to increasing of the effective Fe-Fe and Fe-Au interlayer spacings in Fe_n/Au_n MLS. The example of the model structure used in the calculations is presented in Fig. 8. The structure is composed of the alternating atomic planes of Fe and Au in which one per nine atoms is interchanged by Au and Fe, respectively (the interlayer spacing of 1.915 Å was taken). We found that the moderate substitutional disorder leads mainly to the scaling

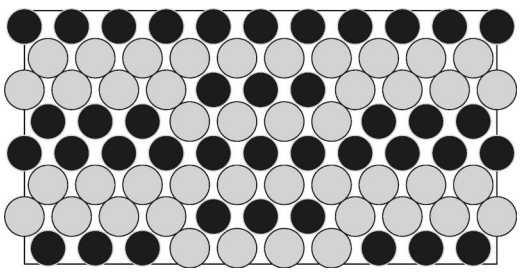

FIG. 7. Unit cell (doubled along *z* direction) of the Fe/Au structure composed of the 1/1 and 2/2 substructures (black spheres are Fe atoms and shadow ones are Au atoms).

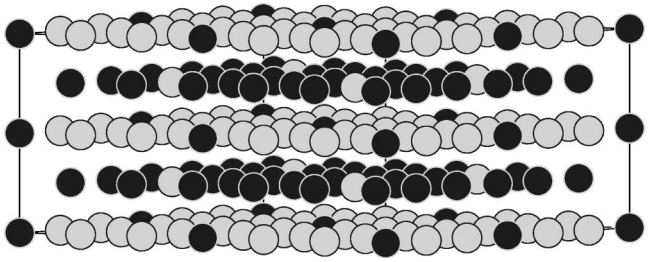

FIG. 8. Doubled $c(3/\sqrt{2}\times 3/\sqrt{2})$ unit cell used for modeling of alloying effect in the Fe/Au MLS (black spheres are Fe atoms and shadow ones are Au atoms).

of the calculated $\sigma^{\parallel}_{\rm off}$ and MOA spectra amplitude, without significant changes of the spectra shape. In Fig. 6(b) the MOA spectra calculated for the model structure (see Fig. 8) are shown. As it is seen, approximately twofold reduction of the MOA magnitude is observed when the level of the substitution is 11%.

Figures 9 and 10 show the experimentally obtained $\omega\sigma^{\parallel}_{\rm off}$ and $\omega\sigma^{\perp}_{\rm off}$ spectra in the MLS of nominal Fe_2/Au_2 and Fe_3/Au_3 structures for two orientations of magnetization: $\mathbf{M}\parallel(001)$ and $\mathbf{M}\perp(001)$, together with the MOA, in comparison with the corresponding spectra calculated for the ideal Fe_2/Au_2 and Fe_3/Au_3 structures. For Fe_2/Au_2 MLS, the overall shape of the theoretical spectra corresponds well to the experimental ones [Fig. 9(b)], and a better agreement in MOA as compared to the previously discussed case of the ideal Fe_1/Au_1 (see Fig. 5) is observed [Fig. 9(c)]. The reason

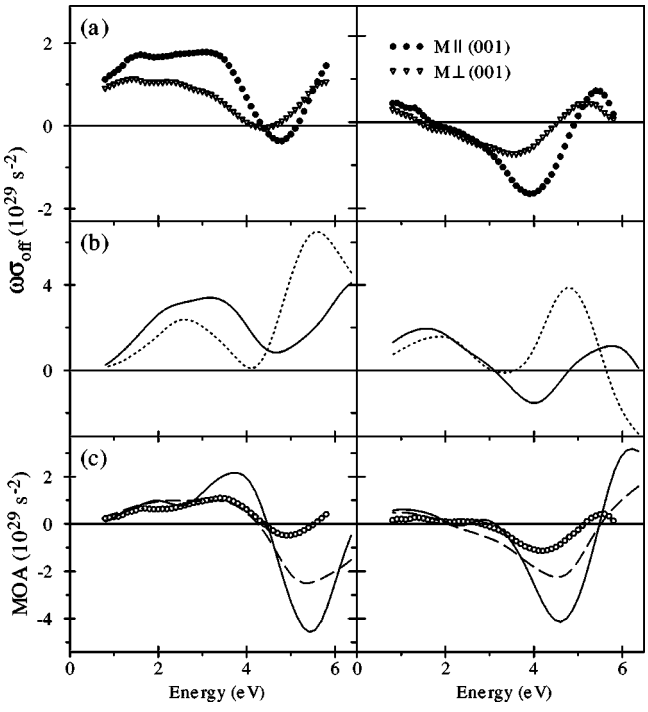

FIG. 9. Absorptive (left panels) and dispersive (right panels) parts of the off-diagonal conductivity tensor of Fe_2/Au_2 MLS; (a) experimental results, (b) LSDA calculated spectra. In the panels (c) the MOA spectra are shown (symbols represent experimental data, solid lines LSDA calculations for perfect Fe_2/Au_2 MLS, and dashed lines calculations for the structure with the substitutional disorder).

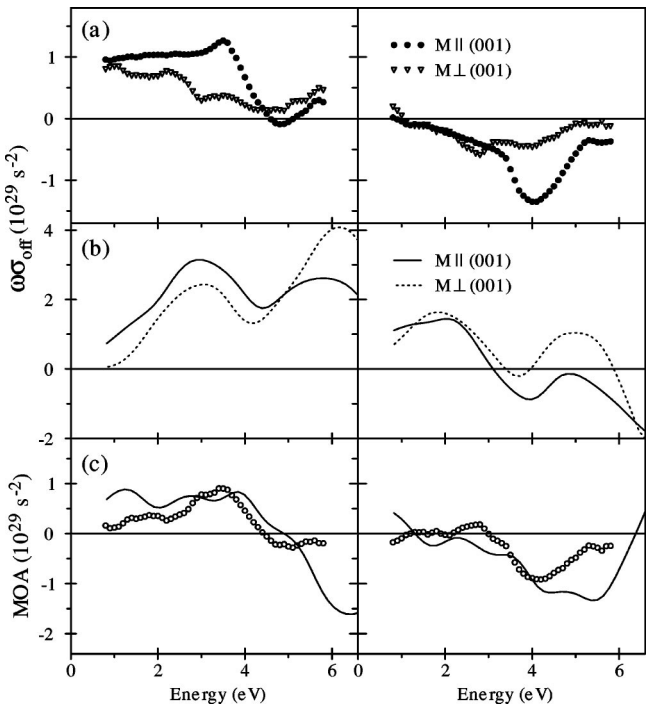

FIG. 10. Absorptive (left panels) and dispersive (right panels) parts of the off-diagonal conductivity tensor of Fe_3/Au_3 MLS; (a) experimental results, (b) LSDA calculated spectra. In the panels (c) the MOA spectra are shown (symbols represent experimental data, solid lines LSDA theory for perfect Fe_3/Au_3 MLS).

is that the ideal Fe_2/Au_2 MLS is a better approach of the real experimental situation than it was in the case of the Fe_1/Au_1 MLS.[18] However, in the high-energy part of the spectra, above 4 eV, the $\omega\sigma^{\parallel}_{\rm off}$ and $\omega\sigma^{\perp}_{\rm off}$ and MOA amplitudes remain considerably higher than the ones obtained experimentally. To examine the origin of such a discrepancy, we have modeled the influence of the substitutional disorder on the MOA in the case of Fe_2/Au_2 MLS. In Fig. 9(c) the MOA spectra calculated for a Fe_2/Au_2 MLS model structure are shown. The model structure used in this case is similar to that considered for the case of Fe_1/Au_1 MLS (Fig. 8) with the same substitutional disorder level and is composed of double numbers of the Fe-rich and Au-rich atomic layers with the experimental modulation period of 7.25 Å. We found that the MOA magnitude for the Fe_2/Au_2 MLS in the high-energy part of the theoretical spectra is markedly reduced and is most close to the experimental ones when the effect of the limited substitutional disorder at the level of the order of 10% is taken into account.

The experimental and theoretical results for the Fe_3/Au_3 structure are presented in Fig. 10. The overall agreement between the calculated and observed $\omega\sigma^{\parallel}_{\rm off}$ and $\omega\sigma^{\perp}_{\rm off}$ spectra for the Fe_3/Au_3 structure is less satisfactory than for the Fe_2/Au_2 MLS. One of the possible reasons is that the real structure of the Fe_3/Au_3 superlattice is far from the ideal model considered. Nevertheless, both the theoretical and the experimental MOA spectra are of comparable magnitudes. The modeling of the interface roughness effects and alloying for the Fe_3/Au_3 structure from first principles (much more complicated than for the simpler structures) is currently in progress.

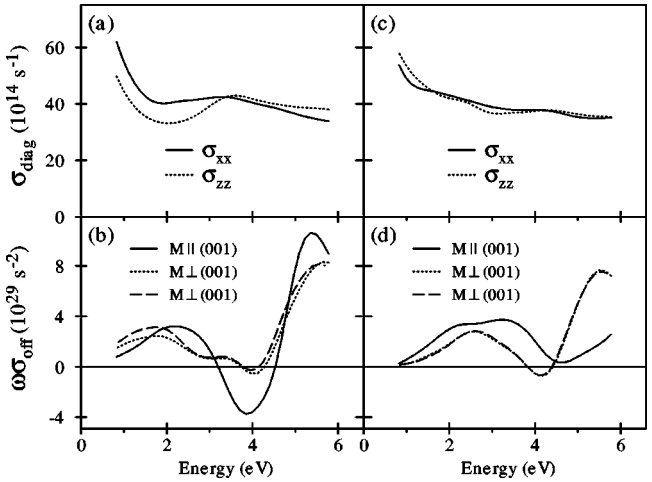

FIG. 11. LSDA calculated absorptive parts of the diagonal σ_{xx} and σ_{zz} (panels a and c) and off-diagonal $\omega\sigma_{\mathrm{off}}^{\parallel}$ and $\omega\sigma_{\mathrm{off}}^{\perp}$ (panels b and d) components of the optical conductivity tensor for Fe_1/Au_1 (left panels) and Fe_2/Au_2 (right panels) MLS. The *ab initio* calculated $\omega\sigma_{\mathrm{off}}^{\perp}$ spectra are represented by dotted lines and the corrected ones by dashed lines (see text).

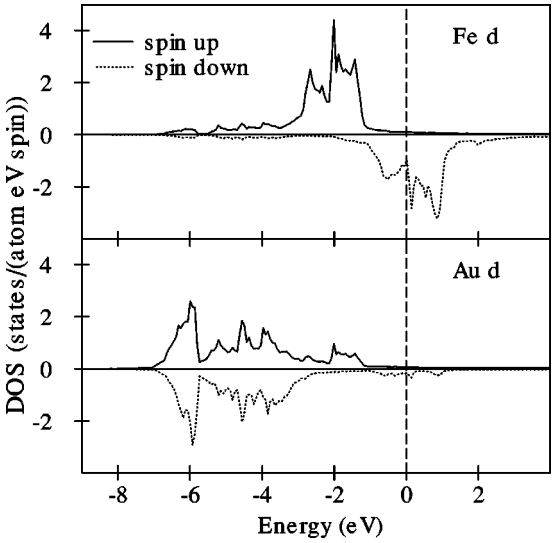

FIG. 12. LSDA spin-projected fully-relativistic partial DOS (in states/(atom eV spin)) of the $L1_0$ ordered Fe_1/Au_1 MLS.

Some conclusions can be drawn from the modeling performed: (i) The magnitude of the off-diagonal optical conductivity and MOA spectra is very sensitive to the actual structure at the interfaces, and thus the MO spectroscopy can provide useful independent information about the Fe/Au MLS structures, complementary to that derived from CEMS measurements. (ii) In the modeling of the roughness effect, even using the areas of the component structures as small as a few atomic spacings leads to the result qualitatively close to that obtained from simple additive formula for the superposition of the spectra. (iii) The magnitude of the MOA decreases with the increase of the number of Fe and Au atomic layers of the superlattices. (iv) The limited substitutional disorder does not suppress the MOA effect in the Fe_n/Au_n MLS.

As it was mentioned in Sec. III, Fe_n/Au_n MLS can exhibit optical anisotropy, but the σ_{zz} component of the optical conductivity tensor is unavailable directly in the experiment. On the other hand, both the σ_{xx} and σ_{zz} can be easily obtained from the calculations and allows us to verify numerically the correctness of using the equation (6) instead of (5) to determine $\omega\sigma_{\mathrm{off}}^{\perp}$ from the experimental data. The absorptive parts of the diagonal components of the conductivity tensor calculated for ideal Fe_1/Au_1 and Fe_2/Au_2 structures are shown in Figs. 11(a) and 11(c). The largest difference between σ_{xx} and σ_{zz} spectra is observed for the Fe_1/Au_1 MLS below the photon energy of about 3.5 eV. For the Fe_2/Au_2 and also Fe_3/Au_3 (not shown in the figure) MLS the calculated optical anisotropy is significantly smaller. The theoretical conductivity tensor components were used to calculate the complex longitudinal Kerr angle according to the exact formula (5). Then, the approximate $\omega\sigma_{\mathrm{off}}^{\perp}$ was derived from the calculated LKE angle using the equation (6) for an isotropic medium. The off-diagonal conductivity spectra recalculated in this way are compared to $\omega\sigma_{\mathrm{off}}^{\perp}$ obtained directly from the *ab initio* calculations in Figs. 11(b) and 11(d). A marked difference between the ''exact'' and ''approximate'' $\omega\sigma_{\mathrm{off}}^{\perp}$ values is observed in the ir range for the Fe_1/Au_1 MLS only. It diminishes to a negligible value above this energy region and can be completely neglected in the whole energy range for the Fe_2/Au_2 and Fe_3/Au_3 structures. The possible errors caused by using the equation (6) instead of (5) are then small and do not affect the conclusion that the large MOA is related to the anisotropy of the off-diagonal conductivity tensor components.

B. Microscopic origin of the magneto-optical and orbital moment anisotropy in Fe_n/Au_n MLS

To understand better the microscopic origin of the MOA let us consider in detail the electronic structure of the Fe_1/Au_1 $L1_0$ MLS. Spin-projected densities of Fe and Au *d* states are shown in Fig. 12 and the calculated spin and orbital magnetic moments are summarized in Table I. Within the Au(Fe) monolayer, each atom is surrounded by four other Au(Fe) atoms at a separation corresponding to the nearest-neighbor spacing in bulk Au(Fe). Due to the smaller number of the nearest neighbors of the same type both Fe and Au *d* states are much narrower than in corresponding

TABLE I. Calculated spin M_S and orbital M_L magnetic moments (in μ_B) of Fe_1/Au_1 versus magnetization direction.

		$\mathbf{M}\parallel[001]$		$\mathbf{M}\perp[001]$	
Atom	State	M_S	M_L	M_S	M_L
Fe	*s*	0.0097	0.0000	0.0098	0.0000
	p	−0.0033	−0.0006	−0.0030	0.0005
	d	2.8593	0.0920	2.8612	0.0587
	f	0.0019	−0.0008	0.0019	−0.0010
	total	2.8676	0.0906	2.8698	0.0582
Au	*s*	−0.0346	0.0000	−0.0345	0.0000
	p	−0.0567	0.0035	−0.0566	0.0058
	d	0.1085	0.0293	0.1098	0.0300
	f	0.0100	−0.0014	0.0100	−0.0016
	total	0.0272	0.0315	0.0287	0.0342

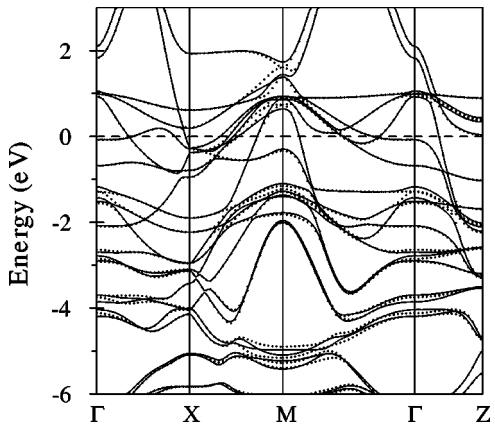

FIG. 13. LSDA energy band structure of the $L1_0$ ordered Fe_1/Au_1 MLS for two orientations of magnetization: $\mathbf{M}\|(001)$ (solid lines), and $\mathbf{M}\perp(001)$ (dotted lines).

bulk metals. As a result the majority spin Fe *d* states are fully occupied which leads to a significant enhancement of Fe spin magnetic moment ($2.87\ \mu_B$) compared to the value of $2.2\ \mu_B$ for bulk Fe. This enhanced magnetization has been observed[16] but the experimental value of $2.75\pm0.25\ \mu_B$ is somewhat smaller than the calculated one. Such a difference can be explained by the deviation of the sample structure from the ideal $L1_0$.

The energy bands in Fe_1/Au_1 MLS calculated for different magnetization directions are shown in Fig. 13. This comparison is useful as it helps to identify the states, which are sensitive to the change of the magnetization direction and, consequently, can potentially give a contribution to MOA, MCA and the anisotropy of the orbital moment. In Fe_1/Au_1 MLS, for example, such states are the electronic states at about -4.0, -2.8, and -1.4 eV in the vicinity of the Γ point and those with energies -5.2, -1.5, and $0.5 \div 1.8$ eV located around the *M* symmetry point as well as along $\Gamma-X-M-\Gamma$ directions.

Comparing the values of the magnetic moments calculated for different magnetization directions one can see from Table I that Fe spin moments are almost independent of the magnetization direction. At the same time the anisotropy of Fe orbital moment, which is determined mainly by Fe *d* states, is quite large and is of the same order of magnitude as it was experimentally observed in Co/Au MLS.[63] This behavior could be expected as in the presence of SO interaction the anisotropy of the orbital moment is of the order of ξ/Δ, where ξ is the SO coupling strength and Δ is the crystal field splitting, while the anisotropy of the spin moment is proportional to $(\xi/\Delta)^2$.[64] As Au *d* states are fully occupied the spin and orbital moments at Au site are small and depend weakly on the magnetization direction.

To understand better the anisotropic behavior of Fe and Au orbital magnetic moments let us introduce a site-dependent function $dm_l(E)$ given by

$$dm_{tl}(E)=\sum_{n\mathbf{k}}\langle\Psi_{tl}^{n\mathbf{k}}|\hat{l}_z|\Psi_{tl}^{n\mathbf{k}}\rangle\,\delta(E-E_{n\mathbf{k}}), \tag{13}$$

where $\hat{l}_z$ is *z*-projection of the angular momentum operator, $E_{n\mathbf{k}}$ and $\Psi_{tl}^{n\mathbf{k}}$ are the energy of the *n*th band and the part of the corresponding LMTO wave function formed by the states with the angular momentum *l* inside the atomic sphere centered at the site *t*, respectively (see Appendix). In analogy to the *l*-projected density of states, $dm_{tl}(E)$ can be referred to as site- and *l*-projected density of the expectation value of $\hat{l}_z$. This quantity has purely relativistic origins and when the SO interaction is equal to zero $dm_{tl}(E)\equiv0$. As van Vleck[65] showed for a free ion, the absence of orbital degeneracy is a sufficient condition for the quenching of the orbital moment, which means that the first-order contribution should vanish: $\langle\Psi_{\mathbf{k}}|\hat{l}_z|\Psi_{\mathbf{k}}\rangle=0$. Thus, the $dm_{tl}(E)$ can be considered as the measure of unquenching of the orbital moment due to the SO interaction.

Furthermore, just as the number of states is defined as the integral of DOS, we can define the integral of $dm_{tl}(E)$

$$m_{tl}(E)=\int_{E_b}^{E}dm_{tl}(E)dE, \tag{14}$$

where E_b is the bottom of the valence band. Then, the orbital moment m_l at the site *t* is given by:

$$m_l\equiv m_{tl}(E_F) \tag{15}$$

(here and henceforth we will drop the index *t* for simplicity).

Both $dm_l(E)$ and $m_l(E)$ are defined in the local coordinate system chosen in such a way that *z* axis is directed along the magnetization and, consequently, they depend on the relative orientation of the magnetization with respect to the crystallographic axes. In the case of Fe_n/Au_n MLS we will use the notations $m_l^{\|}(E)$ and $m_l^{\perp}(E)$ for $m_l(E)$ calculated with $\mathbf{M}\|(001)$ and $\mathbf{M}\perp(001)$, respectively. The difference of these two functions

$$\Delta m_l(E)=m_l^{\|}(E)-m_l^{\perp}(E) \tag{16}$$

can provide useful information on the orientation dependence of the orbital moment. Figure 14 shows the functions $dm_l(E)$, $m_l(E)$, and $\Delta m_l(E)$ calculated for Fe and Au sites in Fe_1/Au_1 MLS. Here and in the rest of the paper we will only consider the contribution coming from *d* orbitals to the m_l related functions. All three functions show strong energy dependence. The variations of the functions at Au and Fe sites are comparable, but Au *d* orbital moment $m_l(E_F)$ is significantly smaller as Au *d*-states are almost fully occupied (see Fig. 12). The anisotropy of the Au orbital moment $\Delta m_l(E)$ vanishes at E_F. At about -1.2 eV Fe $d_\uparrow$ states are already occupied while $d_\downarrow$ are still almost empty (Fig. 12) and, as a result, both $m_l(E)$ and $\Delta m_l(E)$ are zero at this energy. At the Fermi energy, however, we observe strong anisotropy of Fe *d* orbital moment.

To understand better such a behavior let us analyze the orbital character of partial density of Fe *d* states in the vicinity of the Fermi level (Fig. 15). It is worth mentioning that the only nonzero matrix elements of the $\hat{l}_z$ operator calculated between real harmonics with $l=2$ are $|\langle d_{x^2-y^2}|\hat{l}_z|d_{xy}\rangle|=2$ and $|\langle d_{xz}|\hat{l}_z|d_{yz}\rangle|=1$. Hence, the largest contribution to $m_l(E)$ can be expected from the $d_{x^2-y^2}$ and d_{xy} orbitals. Also, it should be pointed out that, in contrast to the case of transition metal films considered in Ref. 4 in which the on-site SO interaction is the only source for the unquenching of the orbital moment, in a compound consisting of 3*d* metal atoms with a large magnetization and a

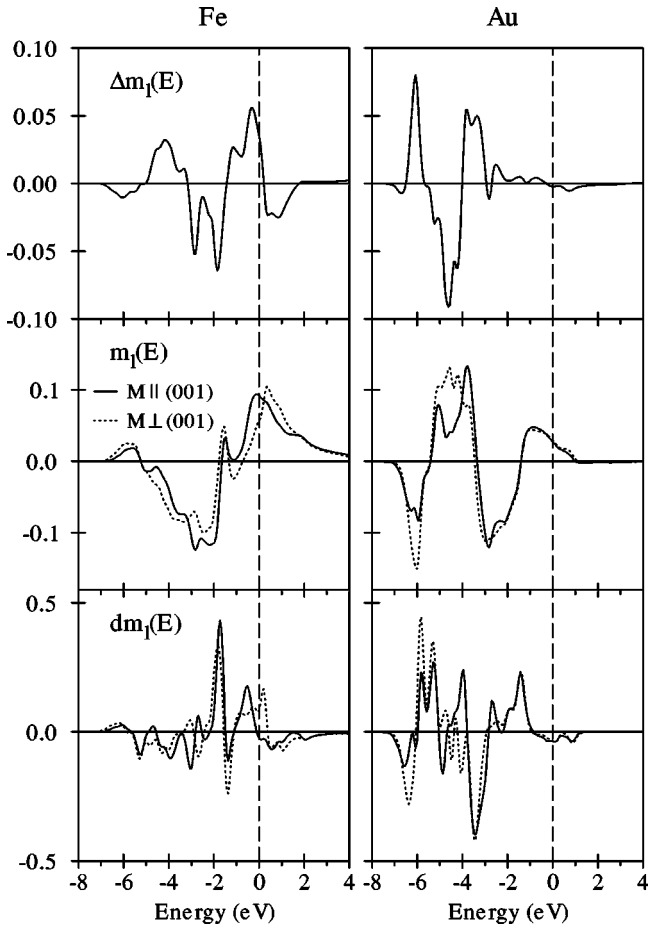

FIG. 14. The $dm_l(E)$ and $m_l(E)$ for two orientations of magnetization together with $\Delta m_l(E)$ for the $L1_0$ ordered Fe_1/Au_1 MLS (see text).

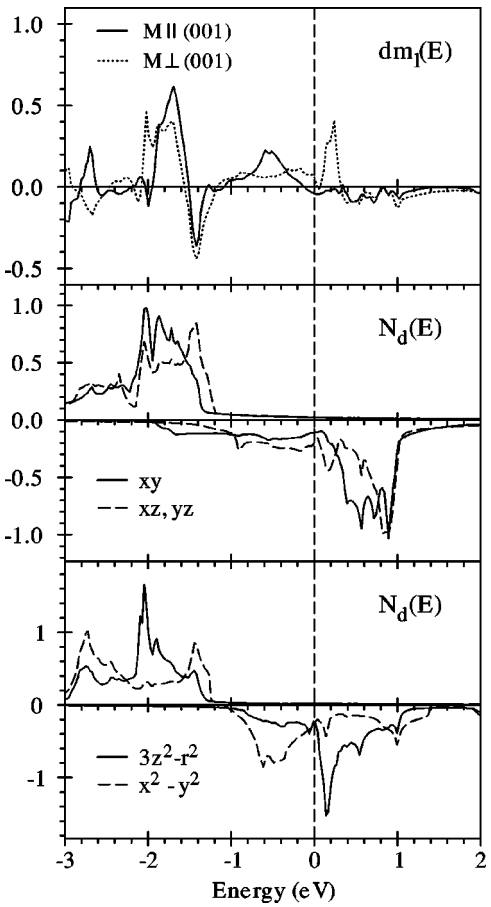

FIG. 15. The *d*-orbitals projected $dm_l(E)$ on Fe site for two orientations of magnetization and *d*-partial density of states (in states/(atom eV spin)) for the $L1_0$ ordered Fe_1/Au_1 MLS.

relatively weak SO coupling and $5d$ atoms for which the SO coupling is strong the unquenching of the $3d$ orbital moment can be caused to a great extent by the $3d-5d$ hybridization. In the particular case of Fe_1/Au_1 MLS there is a peak at -0.5 eV in the density of Fe $d_{x^2-y^2}$ states (Fig. 15) which hybridize rather strongly with Au *d* states. The density of d_{xy} states is constant in this energy interval and, as a consequence, the $dm_l(E)$ has a maximum at this energy for $\mathbf{M}\|(001)$. The states, which form the peak of DOS just above the Fermi level, are predominantly of $d_{3z^2-r^2}$ character and they do not contribute to $dm_l(E)$. When the magnetization direction changes from $\mathbf{M}\|(001)$ to $\mathbf{M}\perp(001)$ the local coordinate system in which $dm_l(E)$ is calculated should also be changed accordingly. In the rotated coordinate system $d_{3z^2-r^2}$ orbital transforms into a linear combination of the $d_{3z^2-r^2}$ and $d_{x^2-y^2}$ orbitals and a sharp peak of $dm_l^{\perp}(E)$ appears above the Fermi level which follows the shape of the corresponding peak of the density of $d_{3z^2-r^2}$ states. At the same time, the $d_{x^2-y^2}$ orbital, which plays the crucial role in the formation of the peak of $dm_l^{\|}(E)$ at -0.5 eV, transforms into $\sqrt{3}/2d_{3z^2-r^2}+\frac{1}{2}d_{x^2-y^2}$ and, as a result of the reduced contribution of the $d_{x^2-y^2}$ orbital to the wave function, $dm_l^{\perp}(E)$ is suppressed below the Fermi level. These simple considerations allow to explain the strong dependence of the Fe orbital moment on the magnetization direction in the Fe_1/Au_1 MLS.

Spin-projected densities of Fe and Au *d* states for Fe_2/Au_2 MLS are shown in Fig. 16 and the calculated spin and orbital magnetic moments are given in Table II. As compared to the results for Fe_1/Au_1 MLS, the change in the local environment and the increase of the number of Fe nearest-neighbors around Fe sites result in broadening of *d* bands and decrease of the calculated Fe spin magnetic moment to 2.79 μ_B. As opposite to the Fe_1/Au_1 MLS where we observed the strong anisotropy of the Fe *d* orbital moment, the Fe_2/Au_2 MLS reveals very small anisotropy in the orbital magnetic moment (Table II and Fig. 17). In Fig. 17 the functions $dm_l(E)$, $m_l(E)$, and $\Delta m_l(E)$ calculated for Fe and Au sites in Fe_2/Au_2 MLS are shown. Although all the three functions show strong energy dependence like in the case Fe_1/Au_1, however, at the Fermi energy we observe negligible anisotropy of Fe *d* orbital moment. The explanation can be found in Fig. 18. In the case of Fe_2/Au_2 MLS there also are two peaks in the partial density of Fe *d* states below and above the Fermi level but in contrast to the Fe_1/Au_1 MLS they have the same $d_{x^2-y^2}$ character (Fig. 18) with a strong admixture of $d_{3z^2-r^2}$. Moreover, the partial weights of $d_{x^2-y^2}$ and $d_{3z^2-r^2}$ states at the Fermi level are such that $m_l(E_F)$ changes only slightly upon the changing of the magnetization direction from $\mathbf{M}\|(001)$ to $\mathbf{M}\perp(001)$ and the anisotropy of the Fe orbital moment $\Delta m_l(E_F)$ is very small (see insert in Fig. 17).

The dependence of the MOA on the SO coupling and

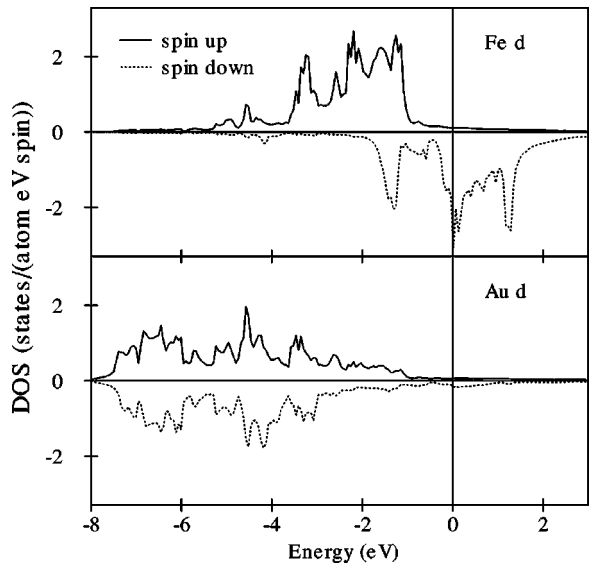

FIG. 16. LSDA spin-projected fully-relativistic partial DOS (in states/(atom eV spin)) of the Fe_2/Au_2 MLS.

hybridization strengths is very complicated (see, e.g., Ref. 66) and does not allow to introduce a simple model consideration as in the case of the MC anisotropy.[3,4] While the anisotropic band splitting can be directly related to the MCA, the situation with MOA is more complex as the eigenvalues and wave functions of both the initial and final states enter the expression for the matrix elements. Therefore, the only way to obtain a realistic description of the MOA is to perform numerical calculations. The optical conductivity can be expressed as a sum of additive contributions coming from interband transitions with the initial and/or final states lying in different nonoverlapping energy intervals. In the case of Fe_1/Au_1, the Fe $d_\uparrow$ and Fe $d_\downarrow$ states are well separated in energy, but overlapped with the Au d states in a wide energy interval (see Fig. 12). Even less distinct separation in the energy position of the initial Fe and Au d states is observed in the case of Fe_2/Au_2 MLS (see Fig. 16). It seems to be more informative to examine the dependence of the MOA on the site-dependent optical transition matrix elements. The calculations have been performed in the way as described in

TABLE II. Calculated spin M_S and orbital M_L magnetic moments (in μ_B) of Fe_2/Au_2 versus magnetization direction.

		$\mathbf{M}\parallel[001]$		$\mathbf{M}\perp[001]$	
Atom	State	M_S	M_L	M_S	M_L
	s	−0.0045	0.0000	−0.0044	0.0000
	p	−0.0192	0.0001	−0.0191	−0.0005
Fe	d	2.8056	0.0835	2.8064	0.0934
	f	0.0084	−0.0013	0.0084	−0.0015
	total	2.7902	0.0824	2.7912	0.0914
	s	−0.0260	0.0000	−0.0259	0.0000
	p	−0.0200	0.0026	−0.0200	0.0036
Au	d	0.0778	0.0155	0.0770	0.0182
	f	0.0059	−0.0009	0.0059	−0.0012
	total	0.0377	0.0172	0.0370	0.0206

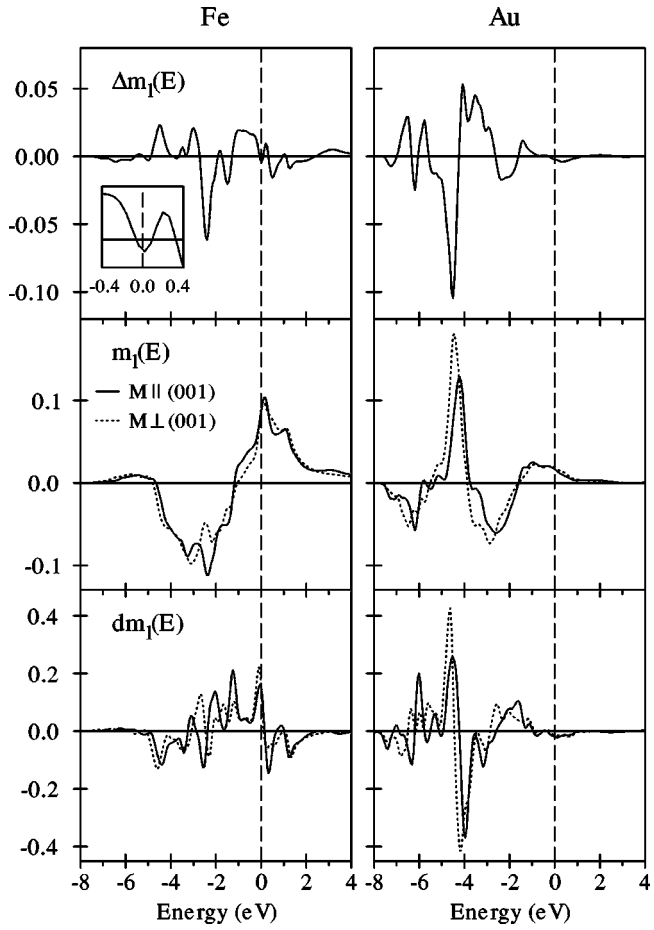

FIG. 17. The $dm_l(E)$ and $m_l(E)$ for two orientations of magnetization together with $\Delta m_l(E)$ for the Fe_2/Au_2 MLS.

Ref. 67, where, within an atomic sphere about either one of the atomic positions, the optical transition matrix elements were set to zero. In this way, the optical conductivity spectra and MOA can be analyzed in terms of the contributions arising from the transitions on the particular sites. The decomposition of the MOA into the contributions from interband transitions on the Fe and Au sites in Fe_1/Au_1 MLS is shown in Fig. 19(a). As it can be seen, the MO anisotropy spectrum magnitude is determined by both the Au and Fe sites, depending on the spectral region. Only in the 0 to ~1 eV energy interval the MOA can be connected exclusively with the transition on the Fe site. The interband transitions on the Au site are mainly responsible for the MOA spectra in the ~1 to ~5 eV energy interval. The transitions occur between the Au $d_\downarrow$ states located at energies $E \leqslant -1$ eV below the Fermi level and the hybridized states of p and f characters lying in the energy range up to 2 eV above the Fermi level. The enhanced density of these final states arises due to the strong hybridization with Fe $d_\downarrow$ states in the energy interval. In particular, the peak at 3.7 eV in MOA spectra is completely determined by these transitions. The peak at 5.3 eV is equally due to both the Fe and Au related transitions. The results of the analysis for Fe_2/Au_2 MLS is shown in Fig. 19(b). As in the case of Fe_1/Au_1 MLS, the transitions on both Fe and Au sites determine resulting MOA spectra in the Fe_2/Au_2 MLS; however, main contribution arises from transitions on the Au site in the whole spectral range. We have

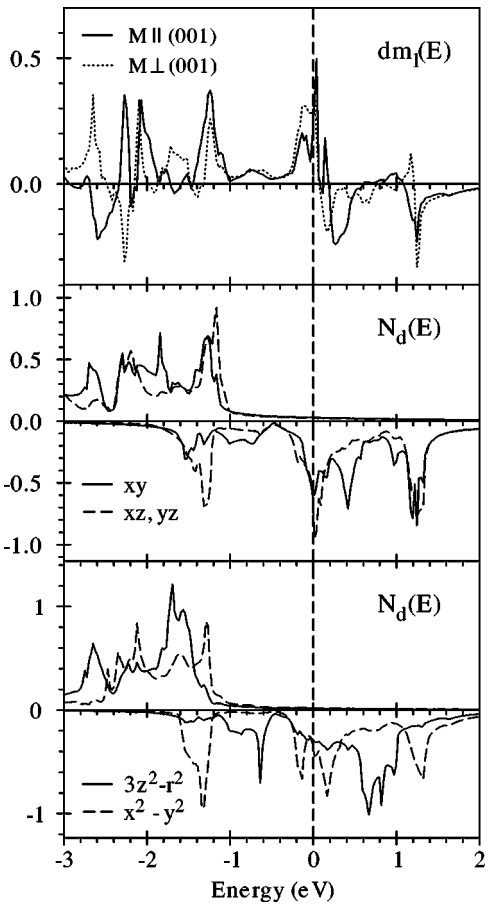

FIG. 18. The $dm_l(E)$ on Fe site for two orientations of magnetization and *d*-partial density of states (in states/(atom eV spin)) for the Fe_2/Au_2 MLS.

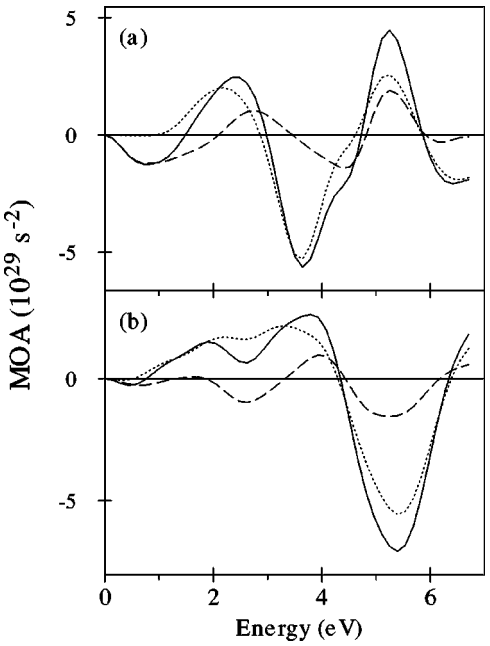

FIG. 19. Decomposition of the calculated MOA spectra (solid lines) into the contributions coming from all interband transitions on Fe (dashed lines) and Au (dotted lines) sites in Fe_1/Au_1 (a) and Fe_2/Au_2 (b) MLS.

verified that the prominent peak in the Fe_2/Au_2 MOA spectra at 5.5 eV is mostly determined by Au *d* related transitions to the final states extended up to ~4 eV above the Fermi level.

Two major effects lead to the appearance of the MOA when the magnetization direction is changed: (i) the change of the band energies (Fig. 13) and (ii) the change of the orbital character of the wave functions. To determine which of the effects dominates we performed two model calculations. In the first one, the spectra were obtained using the as calculated band energies while the corresponding momentum matrix elements at every **k**-point were averaged over the magnetization directions. The calculated MOA is zero in this case, whereas the MOA obtained from the second calculation, in which—vice versa—the averaged band energies and as calculated matrix elements were used, is in a very good agreement with the results of the *ab initio* calculation. It clearly demonstrates that the main effect of MOA comes from the change of the orbital character of the wave functions due to the magnetization axis rotation. This is exactly the origin also the anisotropy of the orbital moment, as discussed before. Although the common origin of both anisotropies is the spin-orbit interaction, the relationship between the orbital moment anisotropy and the MOA is not simple. While the orbital moment anisotropy is determined by the integral property of the occupied states [Eqs. (13)–(16)], the magneto-optical anisotropy is related to the energy dependent quantity being the convolution of all the initial occupied and final unoccupied states within the given energy difference [Eq. (9)].

We examined the dependence of the MOA on the exchange splitting and the SO interaction in the way as in Refs. 33 and 67. We found that the SO coupling of Au is equally responsible for the large MOA as the exchange splitting of Fe. If we set the SO coupling on Fe to zero, the off-diagonal optical conductivity is changed in the whole energy interval by a negative shift similar for both magnetization directions [Figs. 20(a) and 20(b)]. So, the contribution of the SO coupling on Fe site to the conductivity is significant but almost isotropic. As a result, the MO anisotropy practically does not depend on the SO coupling strength on Fe site [Fig. 20(c)]. On the other hand, putting the SO coupling on Au site to zero affects strongly the off-diagonal optical conductivities leading to a strong suppression of the MOA. As in the case of Fe_1/Au_1 MLS, setting the SO coupling on Fe to zero in the Fe_2/Au_2 MLS changes the MO anisotropy to a lesser extent than the off-diagonal optical conductivity (not shown). However, putting the SO coupling on Au site to zero strongly affects both the off-diagonal optical conductivity and the MOA. Thus, the SO coupling of Au is mainly responsible for the large MO anisotropy in the Fe/Au MLS.

V. SUMMARY

The large orientation dependence of the magneto-optical response in the Fe_n/Au_n multilayer structures has been experimentally observed. The magnitude of the magneto-optical anisotropy is very sensitive to the actual atomic structure of the superlattice and decreases as the number of atomic layers of the same type increases. The MOA phenomenon in Fe_n/Au_n MLS and its high sensitivity on the superlattice microstructure was investigated by *ab initio* calcula-

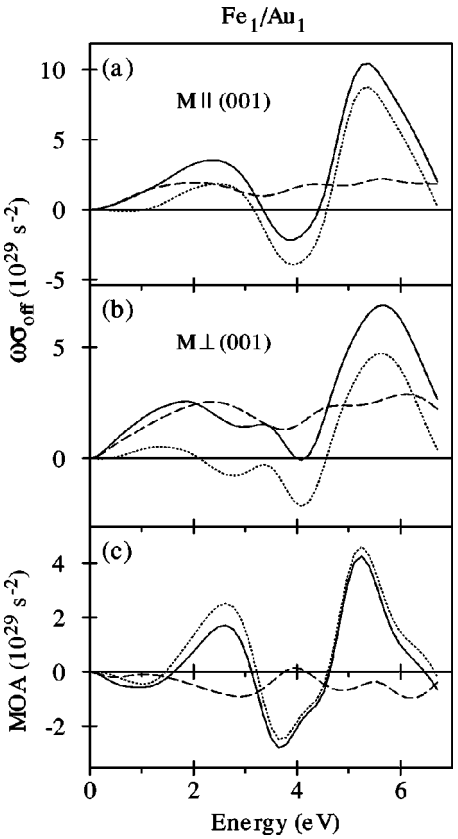

FIG. 20. Calculated absorptive off-diagonal part of the optical conductivity (a,b) and MO anisotropy (c) in the Fe_1/Au_1 MLS (solid lines) together with the results of the calculations for the SO coupling set to zero on Au site (dashed lines) and Fe site (dotted lines).

tions by modeling of the effects of substitutional disorder and the roughness at the interfaces. In the case of the Fe_1/Au_1 MLS the calculations describe well the measured spectra only after taking into account the real structure of MLS, namely, the mixture of mono- and double-layer structures. It was verified that limited substitutional disorder at the interfaces leads to the decreasing of the MO anisotropy.

The orientation anisotropy of the *d* orbital moment was calculated from the first principles. As Au *d* states are almost completely occupied, the spin and orbital moments at the Au site are small and depend weakly on the magnetization direction in the Fe_1/Au_1. At the same time the anisotropy of Fe orbital moment, which is determined mainly by Fe *d* states, is quite large. It was shown that two strong maxima in Fe *d* partial density of states in vicinity of the Fermi level of the Fe_1/Au_1 MLS, which are predominantly of $d_{x^2-y^2}$ character below the Fermi level, and of $d_{3z^2-r^2}$ character just above the Fermi level arise. Such an orbital character of partial density of states leads to the strong anisotropy of Fe *d* orbital moment in the Fe_1/Au_1 MLS. In the case of the Fe_2/Au_2 MLS there are two strong maxima in Fe *d* partial density of states, both being predominantly of $d_{x^2-y^2}$ character. As a result, the change of the magnetization direction leads to almost isotropic Fe *d* orbital moment in the Fe_2/Au_2 MLS.

It is found that the interplay of the strong SO interaction on Au sites and the large exchange splitting on Fe sites through Au *d*-Fe *d* hybridization is responsible for the large MOA and the anisotropy of Fe *d* orbital moment. It is shown that the main effect of the MO anisotropy arises from the changing of the orbital character of the wave functions due to the change of the magnetization direction.

ACKNOWLEDGMENTS

We are indebted to Dr. A.Ya. Perlov for useful discussions during the initial phase of this work. V.N.A. gratefully acknowledges the hospitality during his stay at the Institute of Experimental Physics, University in Bialystok. This work was supported by the Polish State Committee for Scientific Research (KBN) under Contract No. 2 P03B 113 11.

APPENDIX

The function $dm_{tl}(E)$ can be most easily defined when the SO coupling is included in the LMTO Hamiltonian at the variational step. In this case the one center expansion[41] of the LMTO Bloch wave function is given by

$$\Psi^{n\mathbf{k}}(\mathbf{r})=\sum_{tlms}\left(A^{n\mathbf{k}}_{tlms}\phi_{\nu tl}(r_t)+B^{n\mathbf{k}}_{tlms}\dot{\phi}_{\nu tl}(r_t)\right)Y_{lm}(\hat{r}_t)\chi_s, \tag{A1}$$

where $A^{n\mathbf{k}}_{tlms}$ and $B^{n\mathbf{k}}_{tlms}$ can be expressed in terms of the eigenvectors obtained after solving the LMTO eigenvalue problem, $\phi_{\nu tl}(r_t)$ and $\dot{\phi}_{\nu tl}(r_t)$ are the radial solution of the Schrödinger equation in spherically symmetric potential inside the atomic sphere taken at a fixed energy ε_ν and its energy derivative, respectively, $Y_{lm}(\hat{r}_t)$ are the spherical harmonics, χ_s is the eigenfunction of the $\hat{s}_z$ operator corresponding to spin projection *s*, and *tlm* denote the site, the angular momentum, and the magnetic quantum number, respectively. Then, the part of the Bloch wave function formed by the states with the angular momentum l' inside the atomic sphere centered at the site t' $\Psi^{n\mathbf{k}}_{t'l'}$ is given by (A1) with only the terms with $t=t'$ and $l=l'$ left in the sum. This leads to the following expression for $dm_{tl}(E)$:

$$dm_{tl}(E)=\sum_{n\mathbf{k}}\sum_{ms} m\left(|A^{n\mathbf{k}}_{tlms}|^2+|B^{n\mathbf{k}}_{tlms}|^2\langle\dot{\phi}^2_\nu\rangle\right)\delta(E-E_{n\mathbf{k}}), \tag{A2}$$

where we have taken into account that $\hat{l}_z Y_{lm}(\hat{r})=mY_{lm}(\hat{r})$ and $\langle\dot{\phi}^2_\nu\rangle$ is

$$\langle\dot{\phi}^2_\nu\rangle=\int \dot{\phi}^2_\nu(r)r^2\,dr.$$

*To whom any correspondence should be addressed: Email: ubaluba@venus.uwb.edu.pl

†Permanent address: Institute of Metal Physics, 36 Vernadskii str., 252142 Kiev, Ukraine.

[1] For a review on the field of magnetic multilayers, see *Ultrathin Magnetic Structures*, edited by J.A.C. Bland and B. Heinrich (Springer-Verlag, Berlin, 1994), Vols. I and II.

[2] H. Brooks, Phys. Rev. **58**, 909 (1940); G.C. Fletcher, Proc. Phys.

Soc., London, Sect. A **67**, 505 (1954); N. Mori, J. Phys. Soc. Jpn. **27**, 307 (1969); E.I. Kondorskii and E. Staube, Zh. Éksp. Teor. Fiz. **63**, 356 (1972) [Sov. Phys. JETP **36**, 188 (1973)]; J.G. Gay and R. Richter, Phys. Rev. Lett. **56**, 2728 (1986); J.G. Gay and R. Richter, J. Appl. Phys. **61**, 3362 (1987).

[3] P. Bruno, Phys. Rev. B **39**, 865 (1989).

[4] G. van der Laan, J. Phys.: Condens. Matter **10**, 3239 (1998).

[5] See, e.g., J. Trygg, B. Johansson, O. Eriksson, and J.M. Wills, Phys. Rev. Lett. **75**, 2871 (1995); S.V. Halilov, A.Ya. Perlov, P.M. Oppeneer, A.N. Yaresko, and V.N. Antonov, Phys. Rev. B **57**, 9557 (1998), and references therein.

[6] P.M. Oppeneer and V.N. Antonov, in *Spin-Orbit Influenced Spectroscopies of Magnetic Solids*, edited by H. Ebert and G. Schütz (Springer, Heidelberg, 1996), p. 29.

[7] S. Uba, A.N. Yaresko, L. Uba, A.Ya. Perlov, V.N. Antonov, R. Gontarz, and H. Ebert, Phys. Rev. B **57**, 1534 (1998).

[8] Yu.A. Uspenskii, E.T. Kulatov, and S.V. Halilov, Phys. Rev. B **54**, 474 (1996).

[9] E.A. Ganshina, G.S. Krinchik, L.S. Mironova, and A.S. Tablin, Zh. Éksp. Teor. Fiz. **78**, 733 (1980) [Sov. Phys. JETP **51**, 369 (1980)].

[10] R.M. Osgood III, K.T. Riggs, A.E. Johnson, J.E. Mattson, C.H. Sowers, and S.D. Bader, Phys. Rev. B **56**, 2627 (1997).

[11] D. Weller, G.R. Harp, R.F.C. Farrow, A. Cebollada, and J. Sticht, Phys. Rev. Lett. **72**, 2097 (1994).

[12] D. Weller, W. Reim, K. Spörl, and H. Brändle, J. Magn. Magn. Mater. **93**, 183 (1991); K. Sato, H. Ikekame, Y. Tosaka, K. Tsuzukiyama, Y. Togami, and M. Fujisawa, *ibid.* **126**, 572 (1993).

[13] C.-J. Lin, G.L. Gorman, C.H. Lee, R.F.C. Farrow, E.E. Marinero, H.V. Do, H. Notarys, and C.J. Chien, J. Magn. Magn. Mater. **93**, 194 (1991); K. Spörl and D. Weller, *ibid.* **93**, 379 (1991).

[14] H. Kikuchi, Y. Suzuki, and T. Katayama, J. Appl. Phys. **67**, 5403 (1990).

[15] K. Takanashi, S. Mitani, M. Sano, H. Fujimori, H. Nakajima, and A. Osawa, Appl. Phys. Lett. **67**, 1016 (1995); S. Mitani, K. Takanashi, H. Nakajima, K. Sato, R. Schreiber, P. Grünberg, and H. Fujimori, J. Magn. Magn. Mater. **156**, 7 (1996).

[16] K. Takanashi, S. Mitani, K. Himi, and H. Fujimori, Appl. Phys. Lett. **72**, 737 (1998).

[17] K. Takanashi, S. Mitani, H. Fujimori, M. Sato, and Y. Suzuki, J. Magn. Magn. Mater. **177-181**, 1199 (1998).

[18] T. Ślęzak, W. Karaś, M. Kubik, M. Mohsen, M. Przybylski, N. Spiridis, and J. Korecki, Hyperfine Interact. **3**, 409 (1998); J. Korecki, M. Kubik, N. Spiridis, and T. Ślęzak, Acta Phys. Pol. A **97**, 129 (2000).

[19] S. Riedling, N. Knorr, C. Mathieu, J. Jorzick, S.O. Demokritov, B. Hillebrands, R. Schreiber, and P. Grünberg, J. Magn. Magn. Mater. **198-199**, 348 (1999).

[20] K. Sato, E. Takeda, M. Akita, M. Yamaguchi, K. Takanashi, S. Mitani, H. Fujimori, and Y. Suzuki, J. Appl. Phys. **86**, 4985 (1999).

[21] M.E. McHenry, J.M. MacLaren, M.E. Eberhart, and S. Crampin, J. Magn. Magn. Mater. **88**, 134 (1990).

[22] Z.-P. Shi, J.F Cooke, Z. Zhang, and B.M. Klein, Phys. Rev. B **54**, 3030 (1996).

[23] L. Szunyogh, B. Ujfalussy, P. Weinberger, and C. Sommers, Phys. Rev. B **54**, 6430 (1996).

[24] K. Kyuno, J-G. Ha, R. Yamamoto, and S. Asano, J. Phys. Soc. Jpn. **65**, 1334 (1996).

[25] J.-T. Wang, Z.-Q. Li, and Y. Kawazoe, J. Phys.: Condens. Matter **9**, 4549 (1997).

[26] J.-T. Wang, Z.-Q. Li, Q. Sun, and Y. Kawazoe, J. Magn. Magn. Mater. **183**, 42 (1998).

[27] M. Böhm and U. Krey, J. Magn. Magn. Mater. **192**, 27 (1999).

[28] H. Miyazawa and T. Oguchi, J. Phys. Soc. Jpn. **68**, 1412 (1999).

[29] Y. Suzuki, T. Katayama, S. Yoshida, K. Tanaka, and K. Sato, Phys. Rev. Lett. **68**, 3355 (1992); W. Geerts, Y. Suzuki, T. Katayama, K. Tanaka, K. Ando, and S. Yoshida, Phys. Rev. B **50**, 12 581 (1994).

[30] L. Uba, S. Uba, V.N. Antonov, A.N. Yaresko, A.Ya. Perlov, T. Ślęzak, and J. Korecki, Solid State Commun. **114**, 441 (2000).

[31] N. Spiridis and J. Korecki, Appl. Surf. Sci. **141**, 313 (1999).

[32] V. Blum, Ch. Rath, S. Müller, L. Hammer, K. Heinz, J.M. Garcia, J.E. Ortega, J.E. Prieto, O.S. Hernan, J.M. Gallego, A.L. Vazquez de Parga, and R. Miranda, Phys. Rev. B **59**, 15 966 (1999).

[33] S. Uba, L. Uba, A.N. Yaresko, A.Ya. Perlov, V.N. Antonov, and R. Gontarz, Phys. Rev. B **53**, 6526 (1996).

[34] W. Reim and J. Schoenes, in *Ferromagnetic Materials*, edited by K. H. J. Buschow and E. P. Wohlfarth (North-Holland, Amsterdam, 1990), Vol. 5, p. 133.

[35] Š. Višňovský, Czech. J. Phys., Sect. B **34**, 969 (1984).

[36] G. Metzger, P. Pluvinage, and R. Torguet, Ann. Phys. (Paris) **10**, 5 (1965).

[37] W.H. Kleiner, Phys. Rev. **142**, 318 (1966).

[38] A.H. MacDonald and S.H. Vosko, J. Phys. C **12**, 2977 (1979).

[39] H. Ebert, Phys. Rev. B **38**, 9390 (1988).

[40] I.V. Solovyev, A.B. Shik, V.P. Antropov, A.I. Liechtenstein, V.A. Gubanov, and O.K. Andersen, Sov. Phys. Solid State **31**, 1285 (1989).

[41] O.K. Andersen, Phys. Rev. B **12**, 3060 (1975).

[42] V.V. Nemoshkalenko, A.E. Krasovskii, V.N. Antonov, Vl.N. Antonov, U. Fleck, H. Wonn, and P. Ziesche, Phys. Status Solidi B **120**, 283 (1983).

[43] V.N. Antonov, A.Ya. Perlov, A.P. Shpak, and A.N. Yaresko, J. Magn. Magn. Mater. **146**, 205 (1995).

[44] H. Ebert, H. Freyer, A. Vernes, and G.-Y. Guo, Phys. Rev. B **53**, 7721 (1996).

[45] J. Schoenes, in *Materials Science and Technology*, Vol. 3A: *Electronic and Magnetic Properties of Metals and Ceramics*, edited by K.H.J. Buschow, R.W. Cahn, P. Haasen, and E.J. Kramer (Verlag Chemie, Weinheim, 1992), p. 147.

[46] R. Kubo, J. Phys. Soc. Jpn. **12**, 570 (1957).

[47] C.S. Wang and J. Callaway, Phys. Rev. B **9**, 4897 (1974).

[48] V.N. Antonov, A.I. Bagljuk, A.Ya. Perlov, V.V. Nemoshkalenko, Vl.N. Antonov, O.K. Andersen, and O. Jepsen, Low Temp. Phys. **19**, 494 (1993).

[49] A. Santoni and F.J. Himpsel, Phys. Rev. B **43**, 1305 (1991).

[50] U. von Barth and L.A. Hedin, J. Phys. C **5**, 1629 (1972).

[51] V.V. Nemoshkalenko and V.N. Antonov, *Computational Methods in Solid State Physics* (Gordon and Breach, London, 1998).

[52] P.E. Blöchl, O. Jepsen, and O.K. Andersen, Phys. Rev. B **49**, 16 223 (1994).

[53] Y. Suzuki, T. Katayama, P. Bruno, S. Yuasa, and E. Tamura, Phys. Rev. Lett. **80**, 5200 (1998).

[54] J. Zak, E.R. Moog, C. Liu, and S.D. Bader, J. Magn. Magn. Mater. **89**, 107 (1990); J. Zak, E.R. Moog, C. Liu, and S.D. Bader, Phys. Rev. B **43**, 6423 (1991).

[55] K.A. Mills, R.F. Davis, S.D. Kevan, G. Thornton, and D.A. Shirley, Phys. Rev. B **22**, 581 (1980).

[56] E.E. Krasovskii, A.N. Yaresko, and V.N. Antonov, J. Electron Spectrosc. Relat. Phenom. **68**, 157 (1994).
[57] V.I. Anisimov, J. Zaanen, and O.K. Andersen, Phys. Rev. B **44**, 943 (1991).
[58] V.I. Anisimov, F. Aryasetiawan, and A.I. Liechtenstein, J. Phys.: Condens. Matter **9**, 767 (1997).
[59] V.N. Antonov, A.N. Yaresko, A.Ya. Perlov, P. Thalmeier, P. Fulde, P.M. Oppeneer, and H. Eschrig, Phys. Rev. B **58**, 9752 (1998).
[60] L.Uba, S. Uba, A.N. Yaresko, and V.N. Antonov (unpublished).
[61] H. Okamoto, T.B. Massalski, L.J. Swartzendruber, and P.A. Beck, Bull. Alloy Phase Diagrams **5**, 6 (1984).
[62] C.J. Pastor, C. Limones, J.J. Hinarejos, J.M. Garcia, R. Miranda, J. Gomez-Goni, J.E. Ortega, and H.D. Abruna, Surf. Sci. **364**, L505 (1996).
[63] D. Weller, J. Stöhr, R. Nakajima, A. Carl, M.G. Samant, C. Chappert, R. Megy, P. Beauvillain, P. Veillet, and G.A. Held, Phys. Rev. Lett. **75**, 3752 (1995).
[64] J. Stöhr and H. König, Phys. Rev. Lett. **75**, 3748 (1995).
[65] J.H. van Vleck, *Electric and Magnetic Susceptibilities* (Oxford University Press, Oxford, 1932).
[66] H.S. Bennet and E.A. Stern, Phys. Rev. **137**, A448 (1965).
[67] P.M. Oppeneer, V.N. Antonov, T. Kraft, H. Eschrig, A.N. Yaresko, and A.Ya. Perlov, J. Phys.: Condens. Matter **8**, 5769 (1996).